magnetosphere can attain when the IMF points northward.

REFERENCES AND NOTES

1. J. W. Dungey, *Phys. Rev. Lett.* **6**, 47–48 (1961).
2. J. W. Dungey, in *Geophysics: The Earth's Environment*, C. DeWitt, J. Hieblot, A. Lebeau, Eds. (Gordon and Breach, New York, 1963), pp. 505–550.
3. J. D. Menietti, J. L. Burch, *J. Geophys. Res.* **92**, 7503–7518 (1987).
4. Q. Q. Shi *et al.*, *Nat. Commun.* **4**, 1466 (2013).
5. C. Y. Huang *et al.*, *J. Geophys. Res.* **92**, 2349–2363 (1987).
6. C. Y. Huang, J. D. Craven, L. A. Frank, *J. Geophys. Res.* **94**, 10137–10143 (1989).
7. L. A. Frank, J. D. Craven, J. L. Burch, J. D. Winningham, *Geophys. Res. Lett.* **9**, 1001–1004 (1982).
8. L. A. Frank *et al.*, *J. Geophys. Res.* **91**, 3177–3224 (1986).
9. W. K. Peterson, E. G. Shelley, *J. Geophys. Res.* **89**, 6729–6736 (1984).
10. S. E. Milan, B. Hubert, A. Grocott, *J. Geophys. Res.* **110**, A01212 (2005).
11. D. A. Hardy, W. J. Burke, M. S. Gussenhoven, *J. Geophys. Res.* **87**, 2413–2430 (1982).
12. M. S. Gussenhoven, E. G. Mullen, *J. Geophys. Res.* **94**, 17121–17132 (1989).
13. N. Østgaard, S. B. Mende, H. U. Frey, L. A. Frank, J. B. Sigwarth, *Geophys. Res. Lett.* **30**, 2125 (2003).
14. R. C. Fear, S. E. Milan, *J. Geophys. Res.* **117**, A03213 (2012).
15. A. Kullen, M. Brittnacher, J. A. Cumnock, L. G. Blomberg, *J. Geophys. Res.* **107**, 1362 (2002).
16. N. Østgaard *et al.*, *J. Atmos. Sol. Terr. Phys.* **69**, 249–255 (2007).
17. A. Goudarzi, M. Lester, S. E. Milan, H. U. Frey, *Ann. Geophys.* **26**, 201–210 (2008).
18. J. A. Cumnock *et al.*, *J. Geophys. Res.* **116**, A02218 (2011).
19. A. Kullen, in *Auroral Phenomenology and Magnetospheric Processes: Earth and Other Planets*, A. Keiling, E. Donovan, F. Bagenal, T. Karlsson, Eds. (Geophysical Monograph 197, American Geophysical Union, Washington, DC, 2012), pp. 69–80.
20. R. C. Fear, S. E. Milan, *J. Geophys. Res.* **117**, A09230 (2012).
21. A. P. Walsh *et al.*, *J. Geophys. Res.* **118**, 6042–6054 (2013).
22. S. B. Mende *et al.*, *Space Sci. Rev.* **91**, 271–285 (2000).
23. N. A. Tsyganenko, in *Proceedings of the Third International Conference on Substorms (ICS-3)*, Versailles, France, 12 to 17 May 1996 (SP 389, European Space Agency, Noordwijk, Netherlands, 1996), pp. 181–185.
24. C. T. Russell, *Cosmic Electrodyn.* **2**, 184–196 (1971).
25. J. H. King, N. E. Papitashvili, *J. Geophys. Res.* **110**, A02104 (2005).
26. A. N. Fazakerley *et al.*, in *The Cluster Active Archive - Studying the Earth's Space Plasma Environment*, H. Laakso, M. Taylor, P. Escoubet, Eds. (Springer, Dordrecht, Netherlands, 2010), pp. 129–144.
27. H. Rème *et al.*, *Ann. Geophys.* **19**, 1303–1354 (2001).

ACKNOWLEDGMENTS

Work in the UK was supported by Science and Technology Facilities Council (STFC) Ernest Rutherford Fellowship ST/K004298/1 and STFC grants ST/K001000/1 and ST/K000977/1. R.M. is supported by the Belgian Science Policy Office through the Solar-Terrestrial Center of Excellence. French participation in the Cluster project is funded by the Centre National d'Etudes Spatiales (CNES). IMAGE satellite work at the University of California, Berkeley, was supported through a Southwest Research Institute subcontract under NASA contract NAS5-96020. We acknowledge support from the International Space Science Institute through funding of its International Team on Polar Cap Arcs, and we are grateful for discussions with members of the team. Cluster data were obtained from the Cluster Active Archive (http://caa.estec.esa.int/caa/), and the IMAGE FUV data were provided by the NASA Space Science Data Center (http://nssdc.gsfc.nasa.gov/space/). The OMNI IMF data were obtained through NASA's CDAWeb (http://cdaweb.gsfc.nasa.gov/), for which we acknowledge J. H. King, N. Papatashvilli, and the principal investigators of the magnetic field and plasma instruments on the Geotail and Advanced Composition Explorer (ACE) spacecraft. The DMSP particle detectors were designed by D. Hardy of Air Force Research Laboratory, and data were obtained from the Johns Hopkins University Applied Physics Laboratory.

SUPPLEMENTARY MATERIALS

www.sciencemag.org/content/346/6216/1506/suppl/DC1
Supplementary Text
Fig. S1
References (*28*–*38*)
Movie S1

12 June 2014; accepted 19 November 2014
10.1126/science.1257377

BIOPHYSICS

Extreme electric fields power catalysis in the active site of ketosteroid isomerase

Stephen D. Fried,* Sayan Bagchi,† Steven G. Boxer‡

Enzymes use protein architecture to impose specific electrostatic fields onto their bound substrates, but the magnitude and catalytic effect of these electric fields have proven difficult to quantify with standard experimental approaches. Using vibrational Stark effect spectroscopy, we found that the active site of the enzyme ketosteroid isomerase (KSI) exerts an extremely large electric field onto the C=O chemical bond that undergoes a charge rearrangement in KSI's rate-determining step. Moreover, we found that the magnitude of the electric field exerted by the active site strongly correlates with the enzyme's catalytic rate enhancement, enabling us to quantify the fraction of the catalytic effect that is electrostatic in origin. The measurements described here may help explain the role of electrostatics in many other enzymes and biomolecular systems.

Ketosteroid isomerase (KSI) is a small, proficient enzyme with one of the highest known unimolecular rate constants in biochemistry (*1*, *2*), which has prompted extensive study of its mechanism and the catalytic strategies it uses (*3*–*5*). In steroid biosynthesis and degradation, KSI alters the position of a C=C double bond (Fig. 1A) by first abstracting a nearby α proton (E•S ⇌ E•I), forming a charged enolate intermediate (E•I), and then reinserting the proton onto the steroid two carbons away (E•I ⇌ E•P). The removal of a proton in the first step initiates a rehybridization that converts the adjacent ketone group to a charged enolate, an unstable species that is normally high in free energy and so slow to form. The reaction is therefore expected to produce an increase in dipole moment at the carbonyl bond ($|\Delta\vec{\mu}_{rxn}|$), suggesting that KSI may facilitate this reaction by exerting an electric field ($\vec{F}_{enz}$) on this bond that stabilizes it in the intermediate form and the preceding transition state (Fig. 1B). Using vibrational Stark effects, we have measured the electric field that KSI exerts on this C=O bond, providing quantitative experimental evidence for the connection between electrostatics and catalytic proficiency.

The frequencies of certain vibrations (such as the C=O stretch) shift in a linear manner with the electric field experienced by that vibration from its environment, a phenomenon known as the linear vibrational Stark effect (*6*, *7*). Through this effect, we have shown that vibrations can be used as probes of local electrostatic fields. The nitrile group has been widely deployed to measure electric fields inside enzymes and their relationship to mutation (*8*), ligand occupancy (*9*), or conformational changes over the catalytic cycle (*10*). In this study, we have focused on the C=O group of the inhibitor 19-nortestosterone (19-NT) (Fig. 1C), because when 19-NT binds, the C=O group is loaded directly into the catalytic machinery (*11*, *12*). In this way, 19-NT's C=O vibrational (infrared) frequency shift probes the electrostatic environment that the substrate's C=O bond would experience in the active site, except 19-NT cannot react due to the position of the C=C bond.

To calibrate the sensitivity of 19-NT's C=O vibrational frequency to an electric field, we used two complementary approaches. In Stark spectroscopy (Fig. 2, A and B), an external electric field of known magnitude is applied to a frozen glass containing 19-NT, and the accompanying effect on the vibrational spectrum is recorded (*7*). By fitting the Stark spectrum (Fig. 2B) to derivatives of the absorption spectrum (Fig. 2A), the vibration's difference dipole can be extracted: $|\Delta\vec{\mu}_{C=O}|f = 1.39 \pm 0.05$ cm^{-1}/(MV/cm), where f is the local field factor (fig. S1) (*6*, *7*, *13*). A vibration's difference dipole is its linear Stark tuning rate; that is, 19-NT's C=O vibrational frequency shifts ~$1.4/f$ cm^{-1} for every MV/cm of electric field projected onto the C=O bond axis, whether the source of that field is an external voltage (as in Stark spectroscopy) or an organized environment created by an enzyme active site ($\vec{F}_{enz}$) that we wish to characterize. Whenever an external field is applied to a vitreous sample, vibrational bands will broaden because 19-NT molecules (and their C=O bonds) are randomly oriented with respect to the fixed direction of the external electric field (*6*, *7*). By contrast, a vibrational probe will have a fixed orientation with respect to a protein electric field when bound to a protein, and as such the linear Stark effect then produces spectral shifts instead of broadening. The C=O vibration's Stark tuning rate does not appreciably change when C=O accepts a hydrogen bond (fig. S2), implying that the frequency still responds to fields linearly even when C=O participates in stronger interactions, although those interactions themselves are associated with larger electric fields (*14*).

Department of Chemistry, Stanford University, Stanford, CA 94305-1052, USA.
*Present address: Protein and Nucleic Acid Chemistry Division, Medical Research Council Laboratory of Molecular Biology, Cambridge CB2 0QH, UK. †Present address: Physical and Materials Chemistry Division, National Chemical Laboratory (CSIR), Pune 411008, India.
‡Corresponding author. E-mail: sboxer@stanford.edu

Downloaded from www.sciencemag.org on December 18, 2014

We also pursued a second approach to calibrate the sensitivity of 19-NT's C=O frequency shifts to electric fields and to assign these frequencies to an absolute field scale: Specifically, we measured 19-NT's vibrational spectrum in a series of solvents (table S1) and examined the correlation of the frequencies with the solvents' reaction fields, estimated by molecular dynamics (MD) simulations (*14*). As shown in Fig. 2C, 19-NT's C=O band shifts consistently to the red with increasing solvent polarity, from 1690.2 cm^{-1} in nonpolar hexane to 1634.0 cm^{-1} in water, so that the C=O frequency shifts across a 56 cm^{-1} span from solvatochromic effects. The large redshift in water reflects the large electric fields that are created by water's hydrogen bonds (H-bonds). The trend in solvent shifts is strongly correlated with the average electric field that each solvent exerts on the C=O bond (Fig. 2D and fig. S3A); that is, the plot of observed frequency versus computed field is linear (R^2 = 0.99) and its slope corroborates the Stark tuning rate measured by Stark spectroscopy. The ~2-fold difference between the slope of this curve [0.702 cm^{-1}/(MV/cm)] and the measured Stark tuning rate is consistent with the current understanding of the local field effect ($f \sim 2$), based on other vibrational probes and electrostatic models (text S1) (*13*, *14*). The regression line implies that the frequency variation due to different molecular environments can be well explained as a field effect and suggests that we can model 19-NT's C=O peak frequency in terms of the average electric field experienced by the vibration.

When 19-NT is bound to wild-type KSI, the C=O probe engages in short, strong H-bonds with Tyr^{16} and Asp^{103} (*11*, *12*), and its vibrational frequency reflects the electric field at a primary site of charge rearrangement during KSI's catalytic cycle. Notably, the C=O vibration red-shifts to 1588.3 cm^{-1} (Fig. 3A), 46 cm^{-1} further to the red from the peak frequency in water, implying an extremely large electrostatic field. Attributing the frequency shift to the Stark effect, the linear field-frequency relationship of Fig. 2D maps this frequency value to an ensemble-average electric field of –144 ± 6 MV/cm. Although this highly red-shifted frequency lies outside the known linear range from solvatochromism, additional lines of evidence suggest that the C=O vibrational frequency maintains an approximately linear relationship with the field in this regime; neglect of higher-order terms is expected to result in overestimates of the electric field, but by no more than 10% (fig. S4 and text S2). Not only is the C=O band extremely red-shifted in KSI, it is also extremely narrow (Fig. 3A), suggesting a rather rigid environment (*15*) that greatly reduces the dispersion in the electric field. This is very different from what is observed in H-bonding solvents like water that exert large, but also highly inhomogeneous, electric fields because solvent H-bonds can assume a broad distribution of conformations (dashed traces in Fig. 3A and fig. S3, B and C) (*14*). Furthermore, the position of the C=O band in wild-type KSI is situated at the reddest (highest field) edge of the frequencies sampled by the C=O group in water (see the red and dashed traces in Fig. 3A), suggesting that the active site achieves this large field by restricting H-bond conformations to those that are associated with the largest electric fields.

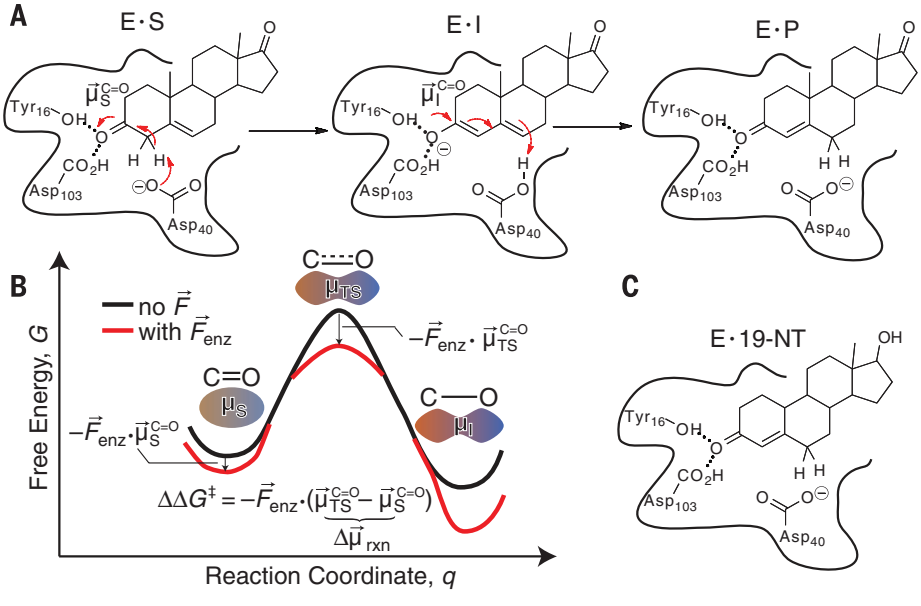

Fig. 1. Catalysis by ketosteroid isomerase. (**A**) The chemical mechanism of ketosteroid isomerase. In the first step, Asp^{40} removes an α proton from the steroid to form an enolate, stabilized by two H-bonds from Tyr^{16} and Asp^{103}. This transformation results in an increase of the dipole moment along the C=O bond. E, enzyme; S, substrate; I, intermediate; P, product. (**B**) Simple model for electrostatic catalysis, illustrating the effect of an electric field from the organized environment of an enzyme active site ($\vec{F}_{enz}$) on a reaction's activation barrier ($\Delta G^{\ddagger}$). $\vec{\mu}_S^{C=O}$, dipole of substrate's C=O bond; $\vec{\mu}_{TS}^{C=O}$, dipole of transition state's C=O bond. (**C**) Complex between KSI and the product-like inhibitor, 19-NT, used in this study to probe electric fields in the KSI active site.

By exploring a series of structurally conservative (but catalytically detrimental) mutants (table S2), we could systematically perturb the catalytic efficacy of KSI and quantitatively evaluate its relationship to the electric field probed by the C=O vibration. In all cases, the assignment of the vibrational bands to 19-NT was confirmed with isotope replacement studies using C=^{18}O 19-NT (figs. S5 and S6). The H-bond provided by Tyr^{16} is known to be essential for KSI's catalysis, as the conservative Tyr^{16}Phe mutation diminishes KSI's rate by factors of ~10^4 (*11*, *16*). This single point mutation induced a blue shift from 1588.3 cm^{-1} to 1647.5 cm^{-1} (Fig. 3A), implying a much smaller average electric field. (This change in field magnitude is comparable to that of the change in solvent field between hexane and water.) The Tyr^{16}Ser mutation (*17*), although less conservative than the Phe substitution, is actually less detrimental. This observation has been explained by the suggestion that leaving a cavity in Tyr^{16}'s place allows water to remain in the back pocket of the active site; these water molecules could also H-bond to the steroid substrate, thereby partially compensating for the loss of Tyr^{16}'s key H-bond (*18*). Indeed, the C=O stretching frequency in Tyr^{16}Ser is not as dramatically blue-shifted as it is in Tyr^{16}Phe. Asp^{103} is the other primary H-bond donor in KSI's active site (Fig. 1A). In the Asp^{103}Asn mutant, the H-bonding proton is much less acidic, but N–H and O–H bonds have similar sterics and dipole moments. Consistent with these considerations, the change in electric field and the rate impairment this mutation entails with respect to wild-type are much smaller compared to the other mutants.

Although it is conventionally accepted that KSI uses Tyr^{16}'s and Asp^{103}'s H-bonds to stabilize its transition state (*1*, *11*), these measurements show that the interaction between these H-bonds and the C=O group can be described fundamentally in terms of the electric field they produce. In all the mutants studied, 19-NT's C=O band remains relatively narrow, suggesting that electrostatic rigidity is conferred by KSI's scaffold, rather than by the H-bonding residues. Also, sizable electric fields persist in the KSI active site after removing the critical H-bond donated by Tyr^{16} (–60 ± 3 MV/cm), implying that a substantial electrostatic field contribution also arises from the environment fashioned by the enzyme scaffold (Fig. 3B). Nevertheless, that the Tyr^{16} H-bond alone contributes a static field of 84 ± 7 MV/cm without an accompanying increase in electric field dispersion makes it quite distinct from water, which donates close to two H-bonds to C=O on average, but taken altogether these H-bonds generate an average field of ~40 MV/cm that is also highly heterogeneous (*13*).

The Asp^{40}Asn mutant decreases KSI's catalytic rate by a factor of ~10^6 (*16*) but only blue-shifts the C=O vibrational frequency of bound 19-NT by 6 cm^{-1} relative to wild-type KSI (table S2). This behavior strongly contrasts with other mutants studied, which produce blue-shifts commensurate with their deleterious effect on catalysis (Fig. 3B). To explain this

observation, we posit that, whereas the function of Tyr[16] and Asp[103] is to stabilize the reaction's transition state by exerting electrostatic fields onto the carbonyl moiety, Asp[40] provides an orthogonal catalytic function (text S3), by acting as the general base in the proton-transfer reaction (Fig. 1A).

When nitrile vibrational probes were placed in other locations around the KSI active site in previous work, frequencies were found well within the range demarcated by the solvent series (*9*). In other words, the extreme electric field experienced by 19-NT's C=O in wild-type KSI is specific to its precise position in the active site where strong local interactions and the collective effect of the overall enzyme architecture mutually reinforce each other.

A plot of each mutant's apparent activation barrier (calculated from the Michaelis-Menten k_{cat}) (fig. S7A) (*16*, *18*, *19*) against its corresponding ensemble-average active-site electric field magnitude (derived from the field-frequency calibration curve in Fig. 2D) reveals a robust linear trend (Fig. 3B; see also fig. S7B). This relationship suggests that electric fields in KSI's active site are intimately linked to catalysis. Moreover, this correlation can be explained using the simple model for electrostatic catalysis in Fig. 1B. The formation of a transition state generally involves redistribution of electron density, resulting in bonds with larger dipole moments than the analogous bonds in the substrate (e.g., $|\vec{\mu}_{TS}^{C=O}| > |\vec{\mu}_{S}^{C=O}|$) (*20*, *21*). An electric field will therefore differentially stabilize the transition state in proportion to the reaction difference dipole ($\Delta\vec{\mu}_{rxn} = \vec{\mu}_{TS}^{C=O} - \vec{\mu}_{S}^{C=O}$), altering the activation barrier by $\vec{F}_{enz} \cdot \Delta\vec{\mu}_{rxn}$ (Fig. 1B). If we make a simplifying assumption that the electric field experienced by the C=O bond is the same in the substrate and transition state, the model can be directly mapped onto the data in Fig. 3B; the slope of the plot (1 D) corresponds to $|\Delta\vec{\mu}_{rxn}|$, and the intercept (18.8 kcal mol^{-1}) corresponds to the hypothetical activation barrier if KSI contributed no stabilizing electric field. The small value for $|\Delta\vec{\mu}_{rxn}|$ implies that there is a rather small perturbation in the electrostatic character of the substrate upon activation, consistent with ab initio density functional theory calculations (fig. S7C and table S3). Apparently, the very large field present in the KSI active site is needed to leverage what small charge displacement is associated with the reaction's transition state. A chemical reaction with a larger charge displacement would consequently be exponentially more accelerated by these electric fields, suggesting that electric field effects may provide a natural framework for explaining the catalysis of more proficient enzymes as well (*22*).

By comparing the intercept extrapolated to $|\vec{F}_{enz}| = 0$ from Fig. 3B (18.8 kcal mol^{-1}) to wild-type KSI's activation barrier (11.5 kcal mol^{-1}), we estimate that the active site's electric field contributes 7.3 ± 0.4 kcal mol^{-1} to KSI's barrier reduction. This corresponds to an ~10^5-fold rate enhancement and accounts for 70% of KSI's catalytic speedup relative to an uncatalyzed reference reaction in solution (Fig. 3C and text S3). Moreover, the electrostatic stabilization energy is quite similar to the enthalpic component of KSI's barrier reduction (9 kcal mol^{-1}), suggesting that the thermodynamic manifestation of the electric field effect is enthalpic (*23*). The active site's suppression of electric field variability, as evidenced by the approximately lifetime-limited linewidth of the C=O vibrational band in all the KSI mutants, is possibly also an important catalytic feature; for example, the Tyr[16]Phe mutant produces a smaller average electric field than water (Fig. 3A), although

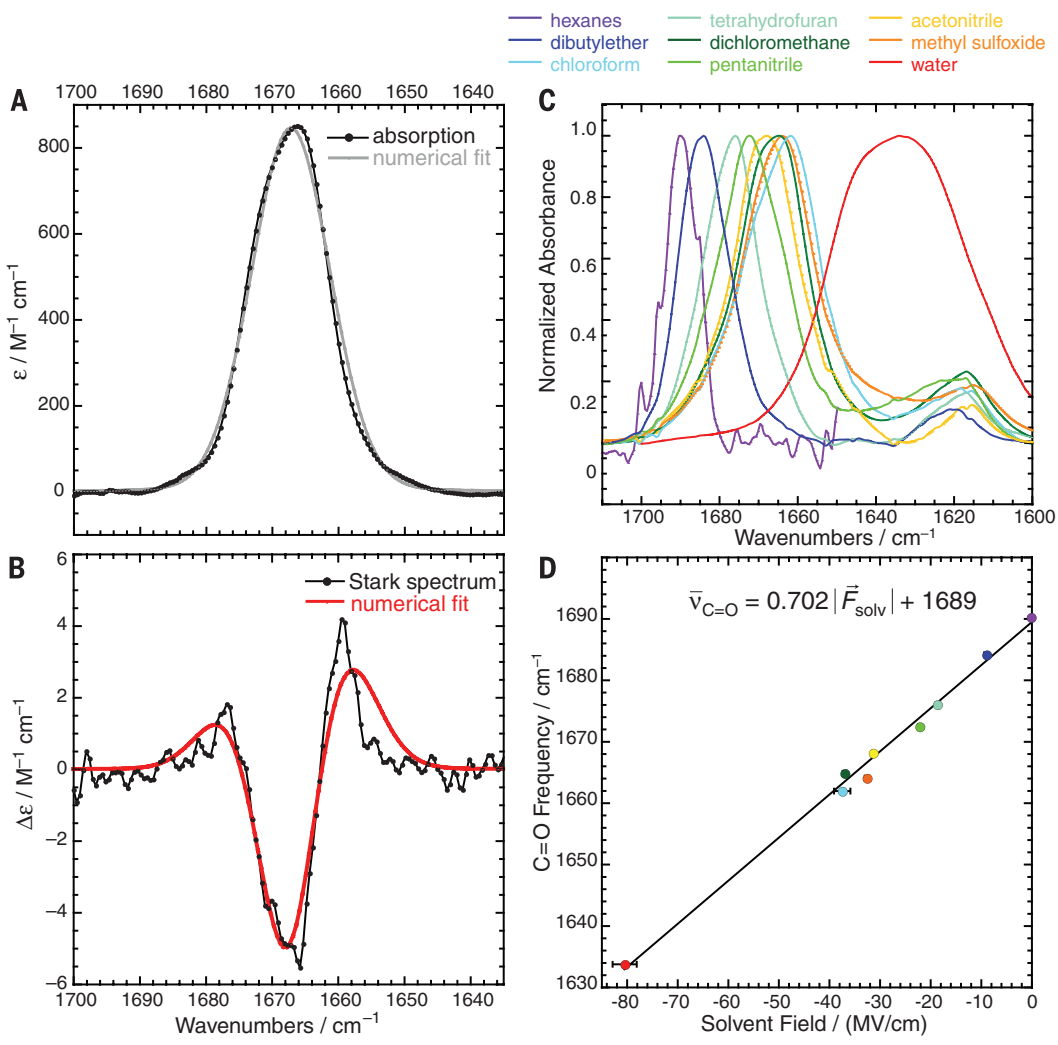

Fig. 2. Sensitivity of the C=O stretch frequency of 19-NT to electrostatic field. (**A**) The absorption spectrum of 19-NT (50 mM) in glassy 2-methyl tetrahydrofuran at 77 K. (**B**) The Stark spectrum of 19-NT at 1.0 MV/cm, shown as a difference between the field-on and field-off spectra. The Stark tuning rate is related to the second derivative fitting parameter (figs. S1 and S2). (**C**) Infrared spectra of 19-NT dissolved in organic solvents of various polarities or water; the small peak at 1615 cm^{-1} is the C=C stretch. (**D**) Plot of 19-NT's C=O peak frequency, $\bar{\nu}_{C=O}$ against the calculated solvent electric field, $|\vec{F}_{solv}|$, the C=O group experiences in each of those solvents (*13*, *14*). The least-squares regression line is $\bar{\nu}_{C=O} = 0.702|\vec{F}_{solv}| + 1689$ (R^2 = 0.99). Error ranges for frequencies are contained within symbols; for electric fields, error bars report the correlation-adjusted error of the average electric field from 2-ns simulations.

it is still a modest catalyst relative to solution. However, the linear infrared experiments described here cannot directly quantitate this effect.

The remaining catalytic effect beyond electrostatics can likely be attributed to the precise positioning of the general base (Asp^{40}) with respect to the proton on the steroid to be abstracted, which is expected to be an entropic effect. From this discussion, we surmise that in enzymatic proton abstraction, electrostatic stabilization and exact positioning of reacting moieties provide the physical basis to achieve enthalpic and entropic contributions to catalysis, respectively; however, contrary to earlier views (*24*, *25*), electrostatic stabilization can be the more important of the two (Fig. 3C).

What is the physical basis for the extreme electric field detected in KSI's active site? Large electric fields arising from Tyr^{16} and Asp^{103} are expected when the carbonyl group of the ligand closely approaches the OH groups of these two residues and in a coplanar orientation [as indeed is seen in crystal (*3*) and solution (*12*) structures]. Nevertheless, these static structures cannot predict or reproduce the electric fields determined by vibrational Stark effects, likely because structures represent ensemble averages and because electric fields depend sensitively on atomic positions down to resolutions not accessible in most structural data (text S4). Moreover, electric fields calculated from classical MD simulations of the KSI•19-NT complex (text S4) also do not agree with our experiments (text S4 and fig. S8). Better estimates of active-site electric fields have been obtained with more sophisticated computational models, which have provided a theoretical foundation supporting the link between electric fields and catalysis (*10*, *21*).

Unusual spectral shifts have been observed previously in enzyme active sites (including KSI) (*11*, *26*–*28*) and have been variously interpreted as implying strain, distortion, or polarization. In contrast, the vibrational Stark effect enables a quantitative connection between spectroscopic observables and a fundamental physical quantity (electric field). As we demonstrate here, these experiments can be applied to measuring the H-bond electric field strength in proteins in functional contexts. Moreover, the electric field description provides a framework to quantify the contributions of specific H-bonding interactions, as well as the overall electrostatic environment with the same units, to give a simple and unified model for electrostatic catalysis (Fig. 1B). That a substantial portion of KSI's catalytic rate enhancement can be explained in terms of its average electric field suggests that the electric field could be a useful design criterion in the ongoing efforts to engineer enzymes with unnatural or enhanced functions. More generally, we anticipate that electric field measurements with functionally relevant vibrational probes will elucidate the physical basis for a broad spectrum of biomolecular and condensed phase interactions and processes.

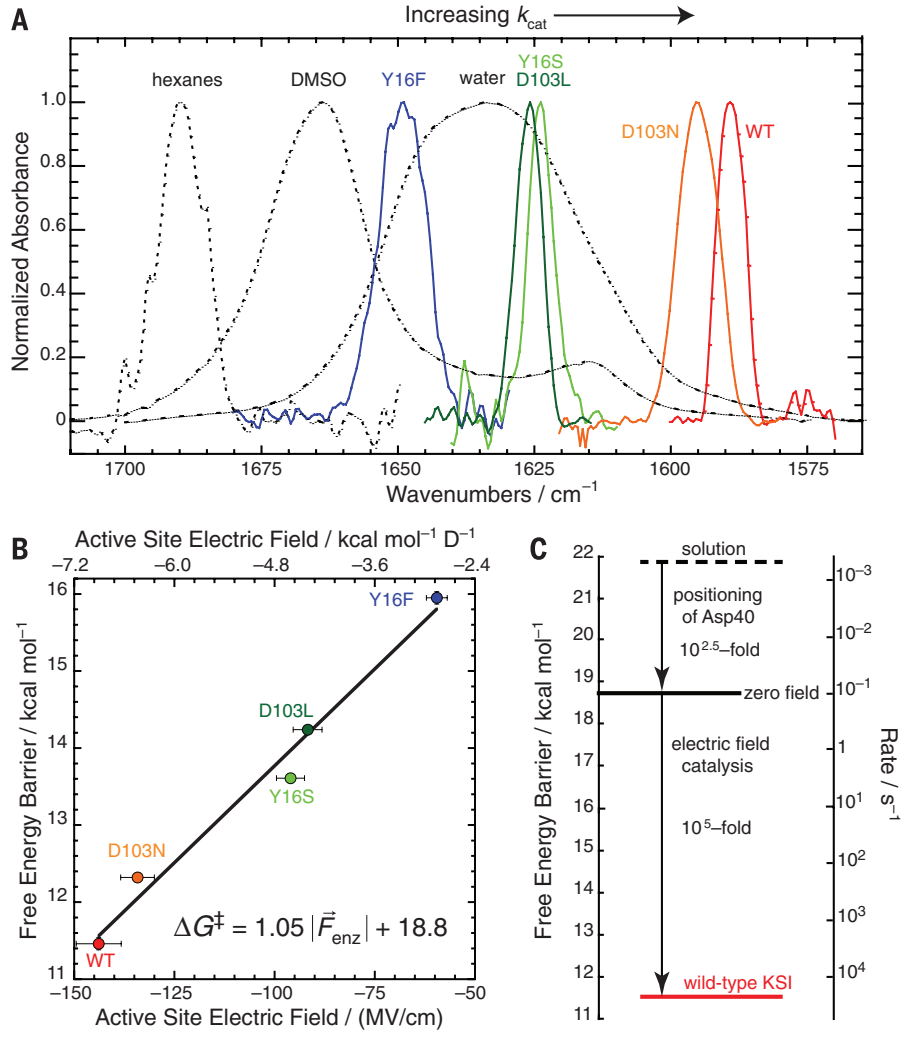

Fig. 3. Contribution of active-site electric fields to KSI's catalytic effect. (**A**) Infrared spectra of 19-NT bound to the active site of wild-type and mutant KSI (color traces), shown alongside a few spectra of 19-NT in solvents (dotted black traces) as a reference. DMSO, methyl sulfoxide; WT, wild type. (**B**) Plot of enzymatic unimolecular free energy barrier, $\Delta G^{\ddagger}$, against the electric field, $|\vec{F}_{enz}|$, 19-NT's C=O group experiences in each of the KSI active sites. Expressing $\Delta G^{\ddagger}$ in kcal mol^{-1} and $|\vec{F}_{enz}|$ in units of kcal mol^{-1} D^{-1} (upper axis), the least-squares regression line is $\Delta G^{\ddagger} = 1.05|\vec{F}_{enz}| + 18.8$ ($R^2 = 0.98$). Error ranges for free energy barriers are contained within symbols; for electric fields, error bars report both experimental error from vibrational frequency measurements and model error from mapping frequencies to electric fields. (**C**) Relative contribution of KSI's catalytic strategies (electric field effect and general base positioning) to speed up KSI's reaction relative to its rate in solution.

REFERENCES AND NOTES

1. R. M. Pollack, *Bioorg. Chem.* **32**, 341–353 (2004).
2. D. C. Hawkinson, T. C. Eames, R. M. Pollack, *Biochemistry* **30**, 10849–10858 (1991).
3. D. A. Kraut *et al.*, *PLOS Biol.* **4**, e99 (2006).
4. S. C. L. Kamerlin, P. K. Sharma, Z. T. Chu, A. Warshel, *Proc. Natl. Acad. Sci. U.S.A.* **107**, 4075–4080 (2010).
5. D. Herschlag, A. Natarajan, *Biochemistry* **52**, 2050–2067 (2013).
6. S. G. Boxer, *J. Phys. Chem. B* **113**, 2972–2983 (2009).
7. S. S. Andrews, S. G. Boxer, *J. Phys. Chem. A* **104**, 11853–11863 (2000).
8. A. J. Stafford, D. M. Walker, L. J. Webb, *Biochemistry* **51**, 2757–2767 (2012).
9. A. T. Fafarman, P. A. Sigala, D. Herschlag, S. G. Boxer, *J. Am. Chem. Soc.* **132**, 12811–12813 (2010).
10. C. T. Liu *et al.*, *J. Am. Chem. Soc.* **136**, 10349–10360 (2014).
11. A. Kuliopulos, A. S. Mildvan, D. Shortle, P. Talalay, *Biochemistry* **28**, 149–159 (1989).
12. M. A. Massiah, C. Abeygunawardana, A. G. Gittis, A. S. Mildvan, *Biochemistry* **37**, 14701–14712 (1998).
13. S. D. Fried, L.-P. Wang, S. G. Boxer, P. Ren, V. S. Pande, *J. Phys. Chem. B* **117**, 16236–16248 (2013).
14. S. D. Fried, S. Bagchi, S. G. Boxer, *J. Am. Chem. Soc.* **135**, 11181–11192 (2013).
15. W. Childs, S. G. Boxer, *J. Am. Chem. Soc.* **132**, 6474–6480 (2010).
16. S. W. Kim, K. Y. Choi, *J. Bacteriol.* **177**, 2602–2605 (1995).
17. G. H. Nam *et al.*, *Biochemistry* **40**, 13529–13537 (2001).
18. D. A. Kraut, P. A. Sigala, T. D. Fenn, D. Herschlag, *Proc. Natl. Acad. Sci. U.S.A.* **107**, 1960–1965 (2010).
19. G. Choi *et al.*, *Biochemistry* **40**, 6828–6835 (2001).
20. A. Warshel, *Proc. Natl. Acad. Sci. U.S.A.* **75**, 5250–5254 (1978).
21. A. Warshel *et al.*, *Chem. Rev.* **106**, 3210–3235 (2006).
22. A. Radzicka, R. Wolfenden, *Science* **267**, 90–93 (1995).
23. W. J. Houck, R. M. Pollack, *J. Am. Chem. Soc.* **126**, 16416–16425 (2004).
24. M. I. Page, W. P. Jencks, *Proc. Natl. Acad. Sci. U.S.A.* **68**, 1678–1683 (1971).
25. J. R. Knowles, *Nature* **350**, 121–124 (1991).
26. J. C. Austin, T. G. Spiro, A. Kuliopulos, A. S. Mildvan, *Protein Sci.* **1**, 259–270 (1992).
27. P. R. Carey, P. J. Tonge, *Acc. Chem. Res.* **28**, 8–13 (1995).
28. J. G. Belasco, J. R. Knowles, *Biochemistry* **19**, 472–477 (1980).

ACKNOWLEDGMENTS

We thank the laboratory of D. Herschlag for providing plasmids of some of the KSI mutants. S.D.F thanks the NSF predoctoral fellowship program and the Stanford Bio-X interdisciplinary graduate fellowship for support. This work was supported in part by a grant from NIH (grant GM27738). S.D.F. designed the study. S.D.F. and S.B. performed experiments and collected data. S.D.F. analyzed the data. S.D.F. and S.G.B. discussed results and wrote the manuscript.

SUPPLEMENTARY MATERIALS

www.sciencemag.org/content/346/6216/1510/suppl/DC1
Materials and Methods
Supplementary Text S1 to S4
Figs. S1 to S8
Tables S1 to S3
References (*29*–*70*)

8 August 2014; accepted 17 November 2014
10.1126/science.1259802

PALEOCEANOGRAPHY

A stagnation event in the deep South Atlantic during the last interglacial period

Christopher T. Hayes,[1,2*] Alfredo Martínez-García,[3] Adam P. Hasenfratz,[3] Samuel L. Jaccard,[4] David A. Hodell,[5] Daniel M. Sigman,[6] Gerald H. Haug,[3] Robert F. Anderson[2]

During the last interglacial period, global temperatures were ~2°C warmer than at present and sea level was 6 to 8 meters higher. Southern Ocean sediments reveal a spike in authigenic uranium 127,000 years ago, within the last interglacial, reflecting decreased oxygenation of deep water by Antarctic Bottom Water (AABW). Unlike ice age reductions in AABW, the interglacial stagnation event appears decoupled from open ocean conditions and may have resulted from coastal freshening due to mass loss from the Antarctic ice sheet. AABW reduction coincided with increased North Atlantic Deep Water (NADW) formation, and the subsequent reinvigoration in AABW coincided with reduced NADW formation. Thus, alternation of deep water formation between the Antarctic and the North Atlantic, believed to characterize ice ages, apparently also occurs in warm climates.

The circulation and biological productivity of the Southern Ocean may help regulate atmospheric CO_2 over millennial to glacial-interglacial time scales (*1*, *2*). Evidence underpinning this view comes largely from study of climate oscillations during ice ages. Here, we report evidence for rapid changes in Southern Ocean circulation during the last interglacial period that is particularly relevant to today's warming climate. Authigenic uranium (aU), a redox-sensitive trace-element proxy for the oxygen content in sediment pore waters (*3*), reveals a millennial-scale reduction in the ventilation of the deep Southern Ocean around 127,000 years ago, when global temperatures were ~2°C warmer than they are today (*4*, *5*).

Most sediment pore water oxygen concentrations are controlled primarily by the balance between diffusive supply from bottom water and consumption by respiration of sedimentary organic matter. We find evidence in samples from Ocean Drilling Program (ODP) Site 1094 (53.2°S 5.1°E, 2807 m water depth, Fig. 1) for changes in deep water oxygen supply by combining aU measurements with controls on the supply of organic matter to the sediments. In this core, the ^{230}Th-normalized biogenic opal flux records changes in the vertical rain of organic matter (*2*, *6*). Lateral supply of organic matter by sediment redistribution, or focusing, is assessed by calculating the focusing factor, Ψ (*7*). For age control during the period surrounding Termination II (T-II), a new sea-surface temperature record from Site 1094, based on the marine lipid index, TEX_{86}^{L}, was correlated to the Vostok ice core δD (*7*, *8*) (Fig. 2A, fig. S1, and table S1).

The penultimate glacial period [marine isotope stage (MIS) 6] at Site 1094 is characterized by low export production (Fig. 2B), typical of the Antarctic South Atlantic during ice ages (*9*). Although substantial sediment focusing occurred during MIS 6 (Ψ = 4, Fig. 2C), these glacial age sediments are low in biogenic opal, our proxy of organic carbon export. Given the absence of an enhanced supply of organic carbon to the sea floor (either vertically or laterally), the aU enrichment during glacial MIS 6 (Fig. 2E) must be due to low bottom water oxygen concentrations, consistent with sluggish ventilation of the Southern Ocean during glacial periods (*10*). This scenario is corroborated by glacial-age aU enrichments observed in other sediment records from the Atlantic (*9*, *11*) and Indian (*12*) sectors of the Southern Ocean.

During the deglacial period (T-II), export production increased rapidly, with ^{230}Th-normalized opal fluxes increasing roughly 10-fold (Fig. 2B). Accounting for concurrent changes in sediment focusing, although aU concentrations decreased (Fig. 2E), the mass accumulation rate (MAR) of aU increased from MIS 6 into the earliest part of T-II (Fig. 2D), consistent with an increased load of organic matter to the sea floor enhancing aU deposition. During the course of T-II, export production remained high or even increased, whereas aU MAR gradually decreased (Fig. 2D). We therefore infer that the gradual deglacial decline in aU MAR was driven by increased oxygenation in deep water as a consequence of increased Southern Ocean overturning during T-II.

Against this backdrop of MIS 6–to–T-II changes that are consistent with previous findings, we observed an entirely unexpected feature in the

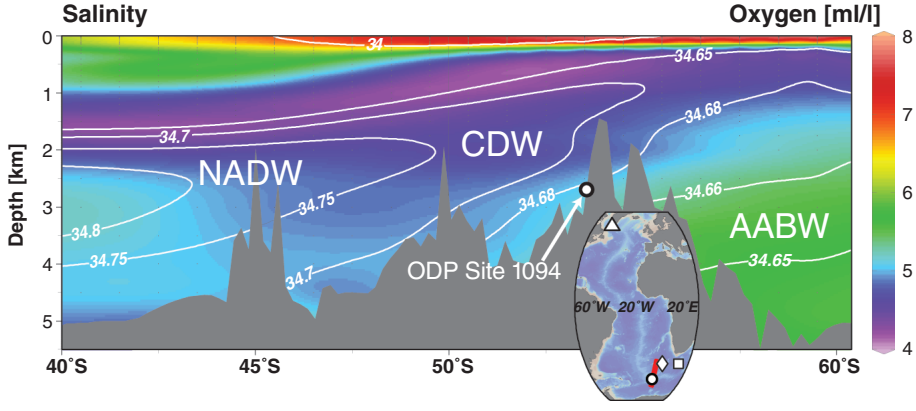

Fig. 1. Vertical section along 5°E in the South Atlantic putting ODP Site 1094 into hydrographic context. Color-mapped oxygen concentrations, with salinity contours overlain, as drawn from the 2009 World Ocean Atlas (*30*, *31*). ODP Site 1094 is marked with a white circle. The inset map indicates the plotted section (red line) and the locations of other cores mentioned in the text: MD03-2664, white triangle; ODP Site 1089, white diamond; and PS2561-2, white square. Figure created with Ocean Data View (odv.awi.de).

[1]Department of Earth, Atmospheric and Planetary Sciences, Massachusetts Institute of Technology (MIT), Cambridge, MA 02142, USA. [2]Lamont-Doherty Earth Observatory of Columbia University, Palisades, NY 10964, USA. [3]Geological Institute, ETH Zürich, 8092 Zürich, Switzerland. [4]Institute of Geological Sciences and Oeschger Centre for Climate Change Research, University of Bern, 3012 Bern, Switzerland. [5]Department of Earth Sciences, University of Cambridge, Cambridge CB2 3EQ, UK. [6]Department of Geosciences, Princeton University, Princeton, NJ 08544, USA.
*Corresponding author. E-mail: cthayes@mit.edu

EXTENDED PDF SPONSORED
BY BIO-TECHNE.COM
bio-techne
LIFE SCIENCE BRANDS
R&D systems NOVUS BIOLOGICALS TOCRIS
LEARN MORE
http://bio-techne.com/launch/?utm_source=Science.com
&utm_medium=PDF%20banner&utm_campaign=Launchv2

Extreme electric fields power catalysis in the active site of ketosteroid isomerase

Stephen D. Fried *et al.*

Science **346**, 1510 (2014);
DOI: 10.1126/science.1259802

This copy is for your personal, non-commercial use only.

If you wish to distribute this article to others, you can order high-quality copies for your colleagues, clients, or customers by clicking here.

Permission to republish or repurpose articles or portions of articles can be obtained by following the guidelines here.

The following resources related to this article are available online at www.sciencemag.org (this information is current as of December 18, 2014):

Updated information and services, including high-resolution figures, can be found in the online version of this article at:
http://www.sciencemag.org/content/346/6216/1510.full.html

Supporting Online Material can be found at:
http://www.sciencemag.org/content/suppl/2014/12/17/346.6216.1510.DC1.html

A list of selected additional articles on the Science Web sites **related to this article** can be found at:
http://www.sciencemag.org/content/346/6216/1510.full.html#related

This article **cites 66 articles**, 8 of which can be accessed free:
http://www.sciencemag.org/content/346/6216/1510.full.html#ref-list-1

This article has been **cited by** 1 articles hosted by HighWire Press; see:
http://www.sciencemag.org/content/346/6216/1510.full.html#related-urls

This article appears in the following **subject collections:**
Biochemistry
http://www.sciencemag.org/cgi/collection/biochem

Downloaded from www.sciencemag.org on December 18, 2014

Science (print ISSN 0036-8075; online ISSN 1095-9203) is published weekly, except the last week in December, by the American Association for the Advancement of Science, 1200 New York Avenue NW, Washington, DC 20005. Copyright 2014 by the American Association for the Advancement of Science; all rights reserved. The title *Science* is a registered trademark of AAAS.

www.sciencemag.org/content/346/6216/1510/suppl/DC1

Supplementary Materials for

Extreme electric fields power catalysis in the active site of ketosteroid isomerase

Stephen D. Fried, Sayan Bagchi, Steven G. Boxer*

*Corresponding author. E-mail: sboxer@stanford.edu

Published 18 December 2014, *Science* **346**, 1510 (2014)
DOI: 10.1126/science.1259802

This PDF file includes:

Supplementary Materials

Table of Contents

I. Materials and Methods:

A. Materials. 19-Nortestosterone (19-NT) and 19-nortestosterone sulfate, sodium salt (19-NT sulfate) were purchased from Steraloids (Newport, RI). Anhydrous solvents and deuterium oxide (99.5% D or higher) were purchased from Acros Organics. All materials were used as received without further purification.

B. Expression and purification of KSI. Wild-type KSI from *Pseudomonas putida* and all mutants were over-expressed in BL-21 A1 cells (Invitrogen), isolated by affinity chromatography using a custom-designed deoxycholate-bound column resin, and purified by gel-filtration chromatography (GE Healthcare) as described previously (*3*). We graciously thank the lab of Daniel Herschlag at Stanford for providing plasmids containing genes for two of the KSI mutants (Y16S and D103L). Following purification, KSI was concentrated to ca. 2 mM, and transferred into buffered D_2O by serial dilution-concentration cycles until the replacement factor exceeded 100. Following replacement into D_2O, KSI was further concentrated to ca. 3–4 mM for FTIR experiments. All KSI genes were verified by standard DNA sequencing (Elim Biopharm), and all KSI proteins were characterized by LC/ESI Mass Spectrometry using maximum entropy deconvolution.

C. Isotopic labeling of 19-Nortestosterone sulfate. A 1–dram glass vial was charged with 1.25 mg of 19-NT sulfate, 90 μL of [^{18}O]H_2O (Cambridge Isotopes, 97 atom% ^{18}O), and 10 μL of glacial acetic acid. 19-NT sulfate fully dissolved upon aspiration with pipette following addition of acid. The vial was sealed and the reaction was allowed to proceed at room temperature for 30 h. The reaction was monitored by taking small aliquots from the vial, diluting with methanol, and performing mass spectrometry. Afterwards, the reaction media was flash-frozen in liquid nitrogen and lyophilized in order to isolate the isotopically-labeled steroid product. [^{18}O]19-NT sulfate was characterized

by LCMS, UV-Vis spectroscopy, and IR spectroscopy. LCMS: mass calc'd for [^{18}**M**] $C_{18}H_{25}O_4{}^{18}OS$ is 356.15. Found: (–) 355.3 [^{18}**M** – ^{1}H]. N.B., a mass of 353.3 [^{16}**M** – ^{1}H] was found on the non-isotopically enriched starting material. UV-Vis: λ_{max} = 248 nm, ε_{248} = 14,000 M^{-1} cm^{-1}; identical to the non-isotopically enriched starting material. IR (10 mM in DMSO): C=^{18}O frequency of 1640.8 cm^{-1}. N.B., that the C=O frequency of the non-isotopically enriched starting material is 1664.7 cm^{-1}. The isotopic replacement yield was estimated at 94% as determined from the relative intensities of the 355/353 signals in ESI (–) and from fitting the IR spectrum to two pseudo-Voigt profiles. This yield is close to the theoretical yield (97%) given the isotopic purity of the reaction medium.

D. FTIR spectroscopy. FTIR spectra were obtained on a Bruker Vertex 70 spectrometer with a liquid nitrogen-cooled mercury cadmium telluride (MCT) detector using methods very similar to that described previously (*14*). A liquid demountable cell was prepared with two windows (CaF_2, 0.750 in thick, Red Optronics) separated using two semicircular mylar spacers (75 μm and 100 μm for studies with organic solvents; 50 μm and 75 μm for studies on KSI). 15–25 μL of liquid sample was injected into the cell, and for volatile solvents, the cell was sealed by wrapping parafilm around the screw caps.

For solvatochromism studies, the samples were prepared by dissolving 19-NT in various liquids to a concentration of 10 mM. 19-NT was soluble to 10 mM in all solvents studied except for hexanes and water. To obtain a spectrum in hexanes, the sample was prepared to saturation (ca. 1 mM). 19-NT was not detectably soluble in water, so to obtain a spectrum in water, the compound 19-NT sulfate was used instead (sulfate replaces the hydroxyl group on the D-ring, see Fig. 1C). Additionally, D_2O was used in place of natural abundance because the H–O–H bending band of H_2O blocks nearly all transmission of light in the C=O-stretching region of the mid-IR. Aside from water, 19-

NT sulfate was also soluble in DMSO, allowing us to compare the C=O frequencies between these two molecules when they are in identical environments. The shift is 0.7 cm^{-1} – negligible relative to the full solvent-induced frequency span, which is over 56 cm^{-1} (table S1). The reference sample in each case was the neat solvent. To acquire a transmission spectrum, the cell was placed in the sample compartment, 5 min was allowed to pass during which atmospheric CO_2 was purged with a nitrogen flow, and then 64 scans of the interferometer were acquired and averaged. The absorption spectra were calculated by subtracting the negative log of the reference transmission from that of the sample transmission.

For studies on KSI, infrared spectra were obtained using samples matched as perfectly as possible using a ligand editing method introduced earlier (*14*) because the protein presents a complex background arising from the amide region which overlaps the C=O band of 19-NT sulfate. KSI was first buffer exchanged into 40 mM potassium phosphate (KP_i) in D_2O, pD = 7.4, and then concentrated to around 4 mM. To prepare samples of KSI for IR spectroscopy, the sample and reference would always be prepared in unison. First, 15 μL of KSI was portioned twice into two separate tubes. Ligand stocks of 19-NT sulfate, [^{18}O]19-NT sulfate, and equilenin (a steroid analog that binds similarly to 19-NT) were prepared at 80 mM in DMSO. Around 0.75 μL of ligand stock was added to the KSI aliquots; the procedure was repeated for the two aliquots, except 19-NT sulfate would be added to one and the reference ligand (either equilenin or [^{18}O]19-NT sulfate) would be added to the other. The liquids were mixed by stirring gently with the micropipette tip. Similarity of preparation between the two samples was found to be of paramount importance to reduce the background signal, which was necessary to observe the desired C=O or C=^{18}O vibrational band.

The typical KSI concentration was around 4 mM, and ligand concentration was around 3

mM. At these concentrations, 19-NT is >99% bound in the active site of WT KSI (K_D of 5 μM) (*29*), and the K_D would have to exceed 150 μM (higher than observed for any mutant) for the percent bound to go below 90%, implying that the detected IR signals of the ligand reflect that of the bound state.

Spectra of the sample and the reference were acquired one after the other. Unlike the samples involving simple solvents, nitrogen purging was carried out for 10–15 minutes, and 256–512 scans were acquired on the interferometer and averaged. Difference spectra were obtained by subtracting the spectrum of the altered ligand (either isotopically or equilenin) from the spectrum of 19-NT sulfate. Clear C=O features were found in spectra for which the intensity of the amide I feature (as either a positive or negative peak) was reduced to 1–5 mOD without further baseline modification (fig. S5A); otherwise, the C=O feature was not distinguishable from the background. Detection of the C=O feature was further facilitated by the particularly narrow linewidth of the band in the KSI active site environment (Fig. 3A).

E. Vibrational Stark spectroscopy. Vibrational Stark spectra were recorded as previously described (*6*, *7*). A brief summary follows: dry 19-NT was dissolved to 50–100 mM in the solvent of interest (or combined with 4 mM WT KSI in 50:50 D_2O:glycer(ol-d_3) to a final concentration of 3 mM) and 3–4 μL were loaded into a custom-designed cell composed of two off-set CaF_2 windows coated with a 4.5-nm layer of Ni metal, displaced by 2 Teflon spacers of 26 μm thickness. Co-solvents for dissolving 19-NT, which can disturb glass formation, were avoided.

The cell was rapidly immersed in a liquid nitrogen-filled cryostat and sealed, after which it was connected to a high-voltage power supply. During acquisition, electric fields in the range of 0.2–1.4 MV/cm were applied, and Stark spectra were obtained by taking the difference between the field-on and field-off infrared transmission spectra. External

electric fields were based on the applied voltage and the distance between the windows (measured by interferometry). The linear Stark tuning rates are extracted through a procedure based on fitting the Stark spectrum to derivatives of the low-temperature absorption spectrum (*6*, *7*).

F. MD simulations in solvents (Fig. 2D). Simulations and electric field calculations of 19-NT dissolved in various organic solvents and water were carried out similarly to previous work on acetophenone (*14*). Briefly: 19-NT was placed at the center of a cubic box filled with solvent molecules, from which 2 nanosecond trajectories were simulated. Snapshots were taken every 200 femtoseconds. From each snapshot, the electric field exerted onto the C=O bond of 19-NT by the solvation environment was calculated. The potential function and the parameters of the generalized AMBER force field (GAFF) were used (*30*, *31*). Simulations were carried out in GROMACS version 4.5.3. (*32*). Electric field calculations were performed according to the prescriptions reported in previous work (*14*). Details about the simulations follow.

F.1. Parameterization. The initial model of 19-NT was built by extracting the coordinates of 19-nortestosterone hemisuccinate from a solution structure of its complex with KSI (PDB: 1BUQ) (*12*). The hemisuccinate moiety was edited off the steroid and a single stereochemical inversion was implemented manually in PyMol. These coordinates were used to create a starting structure of 19-NT to input into the Antechamber program of AmberTools12 (*30*, *31*), which parameterizes organic molecules using the GAFF forcefield and the AM1-BCC procedure to assign atomic charge parameters. For the organic solvent molecules, we used the GAFF parameters of Caleman et al. (*33*), available at www.virtualchemistry.org. Water was modeled using the TIP3P model (*34*).

F.2. Simulations. A cubic box of edge length 5.2 nm was specified around the 19-NT

solute, and filled with solvent molecules using the GENBOX utility in GROMACS and starting coordinates from Caleman et al. (*33*). The solvent boxes were energy minimized with 1000 steps of steepest descent, then equilibrated for 100 ps (2 fs time step) in an NPT ensemble with a reference temperature of 300 K and a reference pressure of 1 bar. In all cases, periodic boundary conditions were applied to the solvent box, and long-range electrostatics were approximated with the particle mesh Ewald (PME) method (*35*), using 1.0 nm as a cut-off. Lennard-Jones interactions were also cut off at distances exceeding 1.0 nm. All bond vibrations were constrained using the LINCS algorithm (*36*). During equilibration, the Bussi thermostat (*37*) and Berendsen barostat (*38*) were active. Production dynamics were carried out for 2 ns in the NPT ensemble, continuing from the final coordinates and velocities of the equilibration run. Temperature-coupling was regulated using a stochastic dynamic integrator (*39*) and the Parrinello-Rahman barostat was applied (*40*). Snapshots consisting of full-precision coordinates and forces were outputted every 200 fs, and used as the basis for electric field calculations.

F.3. Electric field calculations. The electric field experienced by the C=O bond in 19-NT was calculated identically to methods previously described (*14*). For each snapshot, we found the electric field on the C-atom and O-atom of 19-NT's carbonyl moiety, and then projected those fields along the C=O bond unit vector evaluated at the instantaneous geometry. The two numbers were then averaged to yield the instantaneous electric field experienced by the C=O bond, and this process was repeated for each snapshot. The solvent fields reported in Fig. 2D are ensemble averages across the whole trajectory.

G. *Ab initio* calculation of $\Delta\mu_{rxn}$. All *ab initio* electronic structure calculations described here were carried out in Gaussian09 (*41*). A model molecule for 5-androstene-3,17-dione consisting only of the A and B rings of the steroid (terminating the B-ring with

hydrogens at the sites where the fused C ring would connect) was built in GaussView and geometry optimized by density functional theory (DFT) at the B3LYP/6-311++G** level (*42*). This truncated 5-androstene (referred to as 5-andro) was used in place of the full four-ring steroid for computational economy. In PyMol, 5-andro was aligned against the cognate heavy atoms of the ligand (19-nortestosterone hemisuccinate) in the solution structure 1BUQ (*12*). From this aligned frame, the coordinates of 5-andro along with Asp40 up to the beta carbon (effectively truncating it into an acetate ion) were extracted to create a bimolecular supermolecule that recapitulates the active site's geometry between the general base and 5-andro. The bimolecular system was subject to geometry optimization at the B3LYP/6-311++G** level to generate the optimized reactant state (RS – acetate/ketone).

G.1. Locating the transition state (TS). A simple model for the position of the transferred proton in the product state (PS – acetic acid/dienolate) was made by assuming the proton moves along the C_4(5-andro)...O(acetic) vector and that the O(acetic)–H bond length is 0.96 Å. The Cartesian coordinates of the transferred H^+ in the RS and PS were averaged to move the proton to half-way between the two sites. The positions of C_4(5-andro), $H_{4\beta}$, and O(acetic), as well as the bond lengths of C_4(5-andro)...$H_{4\beta}$ and $H_{4\beta}$...O(acetic) were all frozen. The resulting structure was submitted to geometry optimization subject to these constraints at the same level of theory previously employed. This optimization did not converge on the timescales sampled, however after 43 iterations, the coordinates that led to the lowest forces (both maximum and root-mean-square) were taken on to the next step. The coordinates from the previous optimization calculation were subjected to a single-point frequency calculation, which rendered a single negative eigenvalue in the standard orientation. Visualization of the normal mode of vibration that corresponds to the negative eigenvalue corresponded to

motion of $H_{4\beta}$ between C_4 and O(acetic), with concomitant lengthening of C_3=O and planarization about C_4 – in short, recapitulating chemical intuition of the reaction coordinate. Starting with these coordinates, a transition state optimization job (Berny algorithm) was commenced reading in the force constants from the checkpoint file of the frequency calculation (i.e., the `opt=(ts,rcfc)` keyword was used). Additionally the `noeigentest` keyword was necessary to commence the TS search because a second (much smaller magnitude) negative eigenvalue manifests in the non-standard orientation.

G.2. Relaxation from TS to corresponding minima. During the transition state calculation, the acetate fragment swung over considerably with respect to its initial position in RS, rendering unlikely that the initial RS structure is the *closest* minimum to the saddle point located. Therefore, to obtain the nearest minima corresponding to the RS and PS, the TS structure was relaxed off the saddle point by standard optimization. Subjecting the TS to such a calculation quickly furnished a minimum that corresponds to the acetic acid/dienolate species (PS). From this PS, the proton on the acetic-acid was re-positioned onto the C_4 atom of 5-andro with the C_4–$H_{4\beta}$ distance set to 1.10 Å and the $H_{4\alpha}$–C_4–$H_{4\beta}$ angle set to 109.5˚. This initial guess for RS was optimized resulting in a new optimized RS much closer in structure to TS. All of these optimizations were calculated at the B3LYP/6–311++G** level of theory. With these final coordinates of RS, TS, and PS, the atom coordinate root-mean-square deviation between RS and TS is 0.98 Å, and between TS and PS is 0.036 Å.

G.3. Evaluation of electrostatic properties. Single-point calculations calling routines to carry out population analysis were performed on the optimized structures of the RS, TS, and PS at the same (B3LYP/6–311++G**) level of theory. In particular, we used the CHelpG scheme of Breneman (*43*) and the Merz-Kollman scheme (*44*), which both assign atomic charges by fitting against the electrostatic potential. To determine the

local dipole-moment on the C=O bond in the RS, TS, and PS states, we took the average of the absolute value of the charges on the C-atom and O-atom (in *e*), multiplied by the C=O bond length (in Å), and multiplied by 4.803 to convert from *e*Å to D. The critical quantity, $\left|\Delta\vec{\mu}_{\text{rxn}}\right|$, was evaluated by subtracting the C=O bond dipole in the RS from the C=O bond dipole in the TS. The Merz-Kollman scheme was found to give a more physically realistic value, and so was used in the discussion in the main text. The full data set can be found in table S3.

The energies assigned to RS, TS, and PS can serve as qualitative benchmarks of the calculations because of their relationship to kinetic and thermodynamic quantities. ΔE(RS→TS) was found to be 12.44 kcal mol^{-1}, *qualitatively* consistent with the enthalpy of activation ($\Delta H^{\ddagger}$) in solution (16.4 ± 2 kcal mol^{-1}) (*23*). Additionally, ΔE(RS→PS) was calculated to be 10.62 kcal mol^{-1}, in good agreement with the measured ΔH° of 7 ± 2 kcal mol^{-1} for the solution proton transfer reaction (*23*). These findings support the overall reliability of the DFT calculations, and in particular, support the use of a gas phase model to describe the proton transfer process.

H. *Ab initio* calculation of vibrational Stark effects. As with the transition state calculations, 19-NT was modeled in a truncated form that corresponded only to the A and B rings of the 4-ring steroid. The initial model was geometry optimized in the gas phase at the B3LYP/6-311G* level. The optimized structure was re-oriented such that the C=O bond of 19-NT was along the x-axis of the Cartesian coordinate frame; these coordinates were used as an input for 10 separate optimization/frequency calculations, all of which were carried out at the B3LYP/6-311++G** level with anharmonic corrections (*45*). In each calculation, an external electric field directed along the x-axis was specified (with magnitudes ranging from +50 to –150 MV/cm), and the `nosymm` keyword

was included. The molecule's geometry first relaxes to the presence of the field before components of the Hessian matrix are evaluated, which was found to lead to better agreement to experimental Stark tuning rates in previous work (*46*). Following calculations, the C=O stretching normal mode was analyzed.

At zero external field, the potential energy distribution was 90% confined to the C-atom and O-atom, and the displacement vectors were 100% along the CO-axis, supporting the assumption that the vibration is well described as a one-dimensional oscillator. As the field magnitude increased, the mode became more delocalized. At a field of 100 MV/cm, still 81% of the potential energy distribution was confined to the C- and O-atoms and 99.7% of the displacement was along the CO-axis. However, at 150 MV/cm, the mode structure became more complex, with only 50% localization on the C- and O-atoms. The anharmonic frequencies and data are given in fig. S4, A and B.

Supplementary Texts:

1. The local field effect

The effective linear Stark tuning rate of 19-nortestosterone in liquid solution (from comparing solvent-induced frequency shifts to their associated calculated electric fields) is ca. 0.7 cm^{-1}/(MV/cm), which is 2-fold lower than the measured difference dipole of 19-nortestosterone in solid solution from Stark spectroscopy (1.4 cm^{-1}/(MV/cm)). This difference has also been observed for the carbonyl group in acetophenone (*14*). We consider two possible origins for this difference: (1) the local field effect, f (*13*, *47*, *48*), and (2) the possibility that the induced portion of the difference dipole is reflected differently in solvatochromism and Stark spectra due to quadratic Stark effects (see text S2) (*49*). The first effect is more significant than the latter, as will be discussed in the following.

Vibrational Stark spectroscopy involves the application of an external field onto a sample to probe the response of vibrational chromophores to a defined field. For an empty parallel plate capacitor, the electric field is uniform and given by $\left|F_{\text{ext}}\right| = V / d$; it depends only on the voltage, V, and the distance between the two plates, d, which in our experiments are both known accurately (to within about one part in a hundred). When a capacitor is filled with a dielectric material (e.g., a frozen organic solvent), this relationship holds in the macroscopic sense, but microscopically the local electric field created by the external voltage may differ from V / d due to the heterogeneous distribution of polarization induced in the medium by the external charges accrued on the capacitor plates. This local field at a particular point in space will in general differ in direction and magnitude, resulting in $\vec{F}_{\text{local}} = \underline{\underline{f}}\vec{F}_{\text{ext}}$, where $\underline{\underline{f}}$ is a tensor. Previous work has suggested $\underline{\underline{f}}$ is approximately diagonal (*48*), meaning it is well represented as a

scalar (f), but its magnitude is not known experimentally, though several simple physical models have been proposed (*50*). Because of this, Stark spectroscopy does not determine the *microscopic* Stark tuning rate ($\left|\Delta\vec{\mu}_{\mathrm{C=O}}\right|$), but an effective tuning rate modified by the local field correction factor ($\left|\Delta\vec{\mu}_{\mathrm{C=O}}\right| f$). Recent theoretical treatments of the local field effect based on continuum dielectric theory estimated the local field correction factor to be between 1.4–1.8 (SI of *10*). That the slope of 19-nortestosterone's field-frequency relationship in Fig. 2D is about two-fold smaller than the measured Stark tuning rate is consistent with the hypothesis that the tuning rate determined from Stark spectroscopy is enhanced ca. two-fold via the local field effect.

A complete understanding of the local field effect is the subject of ongoing research. We provide here a brief sensitivity analysis discussing how the value of f affects the major conclusions of this work; in particular, if it were close to 1 (as assumed previously (*51–53*)). If we had considered f to be unity, relative electric fields in solvents and KSI could be determined directly from experimental quantities (the observed Stark tuning rate and the frequency shifts), and the resultant electric fields would all be approximately half the values reported in this paper. The rescaling would *not* affect the primary conclusion of this work that KSI's activation barrier correlates well with the active site's electric field, nor would it affect the value of the y-intercept in Fig. 3B (i.e., the extrapolated activation barrier associated with zero electric field) and hence the value given for the electrostatic contribution to KSI's rate enhancement. The value of f *does* however affect the slope of Fig. 3B, and the extracted value given to $\left|\Delta\vec{\mu}_{\mathrm{rxn}}\right|$; namely, if all the electric fields were half the size, then $\left|\Delta\vec{\mu}_{\mathrm{rxn}}\right|$ would be twice its reported value (2 D, instead of 1 D). This would exacerbate rather than assist agreement with the value estimated from *ab initio* calculations (0.5 D); however, we note though that the

theoretical estimate for $\left|\Delta\vec{\mu}_{\text{rxn}}\right|$ is expected to be crude and its value is not the primary focus of this work.

2. Quadratic Stark effects

In the main text, to determine the electric field in the active sites of WT KSI and its mutants, we developed a calibration curve relating 19-nortestosterone's vibrational frequency to electric field using a series of organic solvents and water as reference data. According to MD simulations (and corroborated by the analytic Onsager model, Poisson-Boltzmann models, and fully polarizable atomistic simulations (*13*)), solvation forces in liquid solutions are capable of exerting electric fields whose average values are in the range of 0 to –80 MV/cm. In this range, 19-nortestosterone's vibrational frequency varies strictly linearly with the calculated value of environment's electric field (Fig. 2D). This observation is in accordance with the Stark spectrum (Fig. 2B, fig. S1), which because of its second-derivative lineshape, implies that the C=O vibration possesses a large difference dipole ($\left|\Delta\vec{\mu}_{C=O}\right|$) and a small difference polarizability ($\left|\Delta\underline{\underline{\alpha}}_{C=O}\right|$), responsible for linear and quadratic Stark effects, respectively. It is also consistent with earlier observations (*9*, *54*), that other vibrational probes also demonstrate linear frequency variation with respect to solvent fields.

However, the bathochromic shift induced by the active site of WT KSI is larger than what is observed in organic solvents or even water (Fig. 3A), raising the question of whether vibrational frequency *still* varies linearly with respect to electric field in the range of –80 to –150 MV/cm, to which the solvent series cannot testify. To address this question, we employ *ab initio* density functional theory (DFT) calculations (fig. S4, A and B) and vibrational Stark spectroscopy (fig. S4, C to E).

The overall result of this inquiry (the details of which follows) is that 19-nortestosterone's vibration *does* possess a small quadratic Stark effect, and the first onset of non-linearity begins around water's average solvent field (–80 MV/cm; fig. S4F).

With the electric fields present in the active site of WT KSI, we estimate quadratic Stark effects account for about 20% of the overall frequency shift with respect to the zero-field frequency, and the inclusion of quadratic effects into the field-frequency model lowers the electric field magnitude assigned to WT KSI's frequency from –144 MV/cm to –129 MV/cm (fig. S4F). In other words, extrapolation of the linear calibration curve (Fig. 2D) results in a field overestimated by 10%. Nevertheless, inclusion of quadratic effects into the calibration curve does *not* affect the primary conclusions about the connection between electric fields and catalysis (fig. S7B).

The most straightforward way to investigate quadratic Stark effects in extreme electric fields is by *ab initio* methods, in which arbitrary electric fields can be applied *in silico* and molecular vibrational frequencies can be computed directly. The results from these calculations are shown graphically in fig. S4A and numerically in fig. S4B. The calculated frequencies clearly demonstrate a mostly linear trend in the range of +25 to –50 MV/cm, which is well described with the regression line $\bar{\nu}_{C=O} = 1.0514\left|\vec{F}\right| + 1735.2$ (R^2 = 0.997; N.B. that here and in the following, $\left|\vec{F}\right|$ denotes the electric field C=O experiences, not the field magnitude, and so is signed). Outside this range, parabolic features to the field-frequency curve become more apparent and linear extrapolation of the regression line from the $-50 < \left|\vec{F}\right|/(\text{MV/cm}) < 25$ range results in poor estimation of vibrational frequencies. However, the quadratic regression curve $\bar{\nu}_{C=O} = -0.002915\left|\vec{F}\right|^2 + 0.9344\left|\vec{F}\right| + 1735.3$ describes the frequency variation very well over the full range from –150 to +50 MV/cm (R^2 = 0.9999).

The DFT calculations agree with the solvatochromism studies that 19-nortestosterone's C=O frequency obeys a linear field-dependence in the range associated with organic solvents (0 to –40 MV/cm; Fig. 2B and fig. S3A), but suggest that the linear field-dependence is *not* maintained to large electric fields. In fact, at a field of –150 MV/cm, the linear model assigns a frequency shift that is significantly different (30%) from the quadratic model. However, the DFT calculations do not describe 19-nortestosterone's vibrational frequency quantitatively: they overestimate the zero-field frequency by 46 cm^{-1} and the microscopic Stark tuning rate by 0.35 cm^{-1}/(MV/cm), or about 50%. That DFT systematically overestimates Stark tuning rates by ca. 50% is in line with previous studies and appears to be a fundamental deficiency of single determinant methods (*55*, *56*). Awareness of this deficiency makes us cautious to use DFT's prediction for the quadratic Stark tuning rate, which would likely be even less accurate, as it is a higher-order effect. For instance, DFT predicts (incorrectly) that at the solvent field created by water (–80 MV/cm), 19-nortestosterone's C=O frequency would lie outside the linear regime, which is inconsistent with experiment (Fig. 2D).

A second method to estimate quadratic Stark effects is to use vibrational Stark spectroscopy to measure C=O's difference dipole (*linear* Stark tuning rate) in different environments. In Stark spectroscopy, a small external electric field (ca. 1 MV/cm) is applied to a vibration in addition to the considerably larger matrix field supplied by the environment (ca. 10^2 MV/cm), which can either be a solvent or a protein. In this context, we use the term *matrix* field instead of *solvent* field since in Stark spectroscopy, 19-nortestosterone is encased in a frozen glass instead of diffusing in liquid solution (*57*). Therefore, the Stark tuning rate probed in Stark spectroscopy is effectively the derivative of the field-frequency curve evaluated at the electric field equal to the matrix field, and the matrix field can be determined from the peak frequency of 19-nortestosterone in the

low-temperature absorption spectrum (from a field-frequency model). In a quadratic field-frequency curve, $\bar{\nu}_{C=O} = -\frac{1}{2}a\left|\vec{F}\right|^2 - b\left|\vec{F}\right| + c$, a is the difference polarizability and b is the *intrinsic* difference dipole. In the derivative of the field-frequency curve, $\left|\Delta\vec{\mu}_{C=O}\right| = -a\left|\vec{F}\right| - b$, $-a\left|\vec{F}\right|$ is the *induced* difference dipole, that is, the difference dipole that is created by the matrix field, and b is the linear Stark tuning rate in zero electric field (hence, intrinsic). Therefore, we can probe the quadratic Stark effect (a) by measuring the sensitivity of the linear Stark tuning rate to electric field (environment). By way of contrast, a vibration that has no quadratic Stark effect would have an identical difference dipole in all environments.

We have measured the difference dipole of 19-nortestosterone in a typical organic glass (2-methyltetrahydrofuran; Fig. 2, A and B, fig. S1), in a hydrogen-bonding organic glass (ethanol; fig. S2), and bound to the active site of KSI (fig. S4, C to E). We stress that the latter measurement is qualitative at best for several reasons. Firstly, the analysis of the Stark effect depends on the absorption spectrum, which is reliably obtained in the standard FT-IR experiment by acquiring spectra of carefully matched (isotopically-substituted) samples. The same is not possible in our Stark experiment because the sample cell is destroyed in the experiment. Therefore, the absorption spectrum in fig. S4C is approximate. Moreover, the small number of data points in the narrow spectral region (fig. S4D) precluded the standard lineshape analysis used to extract the difference dipole (*6*, *7*), forcing us to adopt a more qualitative method of extracting the difference dipole that consisted of assuming negligible zeroth- and first-derivative contributions and comparing the intensity of the spectral second-derivative to that of the Stark spectrum (fig. S4E).

In these environments (glassy 2-methyl tetrahydrofuran, glassy ethanol, WT KSI in vitreous water/glycerol), 19-nortestosterone's vibrational frequency redshifts (1667, 1651, 1586 cm^{-1}), which is interpreted as matrices of increasing electric field (–32, –54, –147 MV/cm according to the original linear model function). The linear Stark tuning rate *increases* (1.39 ± 0.05, 1.47 ± 0.1, 1.9 ± 0.25 cm^{-1}/(MV/cm); mean ± std. dev. over three independent experiments for each) across this series, implying a *positive* difference polarizability – i.e., *greater* sensitivity to electric field at higher electric fields. This trend is consistent with the prediction from DFT calculations. Experimental limitations notwithstanding, these studies admit a value for the difference dipole in KSI that is larger than the difference dipole in organic frozen glasses (1.4–1.5 cm^{-1}/(MV/cm)), though not by very much. Less important for our present discussion, the extinction coefficient (related to the transition dipole) consistently decreases (850, 750, 300 $M^{-1}\,cm^{-1}$) across this series implying a negative *transition* polarizability (*7*). It is important to mention that obtaining Stark spectra of 19-nortestosterone bound to KSI proved to be very challenging due to the high background and low signal.

To devise a quadratic field-frequency model (fig. S4F), we examined the relationship between difference dipole and matrix field (determined by inserting the low-temperature absorption peak frequencies into the original linear field-frequency model), admitting a regression of form $\left|\Delta\vec{\mu}_{C=O}\right| = -0.0022\left|\vec{F}\right| + 0.626$ (R^2 = 0.999; N.B. assuming f=2). This equation was integrated to $\bar{\nu}_{C=O} = -0.0011\left|\vec{F}\right|^2 + 0.626\left|\vec{F}\right| + \bar{\nu}_0$ and $\bar{\nu}_0$ was obtained by fitting to the original solvatochromism data. The quadratic field-frequency curve was used to *re*-evaluate the matrix fields, and the calculations described were iterated until the quadratic field-frequency model converged (i.e., it self-consistently describes the relationships among difference dipole, matrix field, and vibrational

frequency); this is given in fig. S4F. Although it is qualitatively similar to the field-frequency curve calculated by DFT (fig. S4A), DFT substantially over-estimated the quadratic Stark tuning rate (by 130%), as originally suspected.

Using the final field-frequency curve, we estimate that the electric field exerted by WT KSI is –129 MV/cm, which differs from the original linear model by 10.4%. Because this difference is quite small and does not appreciably change any aspect of the final analysis (see fig. S7B), we chose to limit discussion in the main text to the linear model for simplicity.

3. Evaluating the electrostatic contribution to catalysis and understanding the Asp40Asn mutant

Questions such as "By how much does an enzyme accelerate a chemical reaction?" and "What portion of the rate enhancement is due to electrostatic interactions?" are old and commonly encountered in biochemistry textbooks. While there is a great deal of experimental information on the former question, there is little experimental information on the latter. The computational literature in this subject is also vast, but is often in conflict and has seldom produced experimentally testable predictions. The results in this paper provide the first direct information on the electric fields in the active site of an enzyme and their connection to catalysis. We claim that the extreme electric field in the active site of wild-type (WT) KSI is responsible for stabilizing the transition state by 7 kcal mol^{-1} (a 10^5-fold rate enhancement) using the simple electrostatic model depicted in Fig. 1B. However, to proceed with statements about what fraction of the total catalytic effect this represents, one must decide upon a suitable reference reaction.

As previously (*58*) we chose the acetate (AcO^-)-catalyzed isomerization of 5-androstene (S) in aqueous solution to be the reference reaction for comparison with KSI's enzyme catalyzed reaction (*59*, *60*). The acetate-catalyzed reaction shares the same chemical mechanism as KSI but differs greatly in its energetics and kinetics (*59*). The bimolecular rate constant for $AcO^- + S \rightarrow AcOH + I$, k^{AcO}, is 6.0×10^{-4} M^{-1} s^{-1} (*59*), and the k_{cat} of WT KSI is 2.4×10^4 s^{-1} (*16*, *61*). The ratio of these numbers, 4×10^7 M, can be regarded as the "effective molarity" of acetate in the vicinity of 5-androstene when in the KSI•5-androstene (E•S) complex (*60*).

As pointed out by Jencks though, this is an unattainable concentration, and so the rapid rate of the intramolecular enzymatic reaction must be ascribed to factors other

than local concentration (*60*). Here we have the opportunity to point out that the 100,000-fold rate effect we have assigned to electrostatic stabilization is unrelated to the local concentration, and so accounting for this, we are left with an effective acetate concentration of 400 M, a value which can sensibly be attributed to the combination of increased local concentration (which can contribute up to 55 M-effect) and rotameric selection. By comparing the total rate enhancement (4.0×10^7 M) to the electrostatic rate enhancement ($10^{5.3 \pm 0.3}$) on a log basis, one calculates electrostatics account for 70 ± 4 % of KSI's barrier reduction, though the molarity scale introduces an arbitrary factor into the comparison (*60*).

This analysis ends up to be numerically equivalent (but semantically different) from the way Warshel and co-workers frame the problem (*21*), wherein enzyme and solution rates are typically compared by subtracting $\Delta G^{\ddagger}_{cat}$ (the activation barrier for E•S → E•I) from $\Delta G^{\ddagger}_{w}$ (the activation barrier of the reference reaction $AcO^- + S \rightarrow AcO^- + I$) (*62*). The activation barriers are derived from the same two rate constants (k_{cat} and k^{AcO}) stated above, and admit a $\Delta\Delta G^{\ddagger}$ of 10.4 kcal mol^{-1} (corresponding to the same rate enhancement).

Two notes must be made about the applicability of k_{cat} and k^{AcO} to the mechanism under consideration. Firstly, k^{AcO} corresponds to the reaction $AcO^- + S \rightarrow AcOH + I$. However, the solution decomposition of intermediate ($AcOH + I \rightarrow AcO^- + P$) is very fast ($2.6 \times 10^3$ M^{-1} s^{-1}) (*59*), which means that the overall rate of $AcO^- + S \rightarrow AcO^- + P$ is also effectively equal to k^{AcO}.

Secondly, in the Michaelis-Menten model, k_{cat} corresponds to the process E•S → E + P; therefore, the k_{cat} of KSI is a composite of rate constants for three microscopic processes: the enolization reaction (E•S → E•I), the reketonization reaction (E•I → E•P), and product release (E•P → E + P). It is generally believed that the enolization reaction

is rate-limiting (*63*, *64*), although there is some evidence that in WT KSI, enolization is fast enough that reketonization (*1*) and product release (*2*) are also partially rate-limiting. The ideal comparison would be between k^{AcO} and the *microscopic* rate constants for E•S → E•I for each of the mutants. In practice, microscopic rate constants have only been evaluated for WT KSI (and from a different homolog) (*2*), whereas Michaelis-Menten k_{cat} values have been accurately determined for all mutants examined. In the main text and in Fig. 3B, activation barriers were calculated on the basis of each enzyme's k_{cat}. We believe k_{cat} is a reasonable proxy for the rate of the reaction E•S → E•I because enolization is rate-limiting for the KSI mutants studied and enolization is partially/mostly rate limiting for WT KSI. Moreover, since k^{AcO} is effectively the rate constant for the full reaction $AcO^- + S \rightarrow AcO^- + P$, it is quite appropriate to compare it to k_{cat} (which corresponds to E•S → E + P).

To make quantitative comparisons between the rates of KSI mutants in terms of an electrostatic model, it is imperative that the mutants all use the same mechanism as the reference reaction and be structurally similar to WT KSI. To this end, KSI is an ideal system because its scaffold is quite rigid, and its structure is relatively robust to perturbation from mutations. In particular, x-ray structures are available for the four mutants (Tyr16Phe, Tyr16Ser, Asp103Asn, Asp103Leu) selected for analysis, and their RMSD's to WT are 0.14–0.38 Å for the whole enzyme, and 0.18–0.32 Å for the active site residues (*18*, *19*, *65*, *66*). The mutants also possess very similar K_M-values (within a factor of 2 from WT), suggesting a conserved binding mode with substrate (*17*, *19*).

The Asp40Asn mutant is important to consider because it results in the largest rate impairment (10^6-fold) of all the mutants considered (*16*) while also resulting in the smallest blue-shift of 19-nortestosterone carbonyl's frequency relative to WT among all the mutants (6 cm^{-1}). Taken at face value, this result could be interpreted as

contradictory evidence to the rate-electric field relationship (Fig. 3C); on the other hand, the result can be understood by considering that Asp40 does not impact catalysis through electrostatic stabilization of the transition state, but by providing a general base to initiate proton abstraction. That Asp40Asn introduces a relatively small infrared frequency shift at the C=O vibrational probe demonstrates that general base catalysis and electrostatic catalysis are complementary and separate roles of the active site.

A related question is that if ablation of Asp40 decelerates KSI's catalysis by 10^6-fold, and the electrostatic effect of Asp40 is minimal, then how can electrostatics, which contributes a ~10^5-fold rate enhancement (from extrapolation of Fig. 3C), be considered the dominant contributor to KSI catalysis? The answer to this lies in the choice of the reference reaction. While Asp40Asn is enormously damaging to KSI's rate, it also alters KSI's mechanism (*67*), which makes it incomparable to the chosen reference reaction. In particular, the identity of the base in the Asp40Asn-catalyzed reaction becomes a hydroxide ion from solution (rather than Asp40), and the reketonization reaction becomes strongly rate-limiting over enolization.

In summary, the adoption of the acetate-catalyzed reaction as the reference reaction enables comparisons to other mutants which maintain the same mechanism; however, it does not allow for incorporation of Asp40Asn into the rate-field model.

4. Calculating electric fields in KSI and implications for the role of dynamics

The electric field at a given point in space is fully determined by the coordinates and charges of all the particles in a system. X-ray structures provide a high-resolution set of atomic coordinates, and conventional force fields assign charges to all those atoms. Therefore, a natural and appealing way to calculate the electric field KSI's active site exerts onto the C=O bond of the 19-nortestosterone inhibitor consists simply of modeling the active site with static point charges placed on the crystallographic coordinates.

As an illustration of this style of modeling, we used the x-ray crystal coordinates of a reduced active site region (consisting of Asp103, Tyr16, and the steroid ligand) from the 1.1-Å resolution structure 1OH0 (*68*), optimized the hydrogen positions using the PDB2GMX module of GROMACS (*32*), and modeled the bond dipole moments on Tyr16 and Asp103 using the atomic charges on the O- and H-atoms of the AMBER force field (*69*). In the original x-ray structure, the $O_{19\text{-}NT}\bullet\bullet\bullet O_{Tyr16}$ and $O_{19\text{-}NT}\bullet\bullet\bullet O_{Asp103}$ distances are both 2.5 Å, and these distances both expand to 2.6 Å once hydrogen atoms are inserted and the energies relaxed. Calculating electric fields with this geometry and Coulomb's law, we found that the OH groups of Tyr16 and Asp103 exert fields of 30.2 MV/cm and 60.9 MV/cm respectively onto the carbonyl group of 19-nortestosterone. The fields are very different despite similar O•••O distances because the Asp103 O–H bond vector is more coplanar with the C=O bond vector. These values can be compared to the shift in the electric field between WT KSI and the Tyr16Phe mutant (84 ± 7 MV/cm) and the Asp103Leu mutant (52 ± 7 MV/cm), respectively, which ablate the electrostatic interaction from the OH group but maintain the overall steric pattern. Although the agreement between calculation and experiment is fair for Asp103, the model does not

capture the large electric field supplied by Tyr16 and incorrectly predicts that Asp103 is electrostatically the more important residue.

This simple analysis illustrates why precise electrostatic information in enzyme active sites cannot be accurately determined from crystal structures – even those that are ultra-high resolution. The reason for this is that electric fields are extremely sensitivity to geometry at even a few percent-of-an-Å length scales and especially to the positions of hydrogens (which are the atoms that get closest to neighboring molecules) – details that are inaccessible to conventional structural biology methods. Moreover, proteins are not static and x-ray structures do not necessarily represent the most typical conformation of a protein in solution. Computer models that account for all interactions in a protein and average over many conformations are necessary, and such is achieved practically by way of MD simulation.

However, MD simulations of the WT KSI•19-nortestosterone complex (modeled with the AMBER99SB-ILDN force field (*69*)) initiated from the same 1OH0 crystal structure also were unable to reproduce the extreme electric field at the C=O bond of 19-nortestosterone. The mean electric field from a 10 ns trajectory was around –60.4 MV/cm (fig. S8, A and B displays the trajectory and histogram), very different from the experimental value (ca. –140 MV/cm), and even smaller than the simulated electric field in water.

Upon visualization, it was not difficult to discern why the simulated fields were so low. We expect the C=O bond to experience large electric fields when it closely approaches the O–H dipoles of the key active site residues, Tyr16 and Asp103. However, during the simulation these close-contact geometries were relatively rare. 19-nortestosterone was frequently found far away from the active site residues over the

trajectory, with an overall mean distance between the hydroxylic O of Tyr16 and the carbonyl O of 19-nortestosterone ($O_{19\text{-}NT}\bullet\bullet\bullet O_{Tyr16}$) distance of 5.5 Å (fig. S8C).

These observations suggest that the AMBER force field does **not** energetically favor a tight hydrogen-bonding geometry between 19-nortestosterone and the key catalytic residues. This supposition is verified from inspecting the van der Waals parameters of the AMBER force field: the van der Waals radius (σ_{ij}) for the $O_{19\text{-}NT}\bullet\bullet\bullet O_{Tyr16}$ pair-wise interactions is 3.01 Å, and given ε_{ij} = 0.21 kcal mol^{-1}, the optimum distance (with respect to this single interaction) is 3.35 Å, and at the crystallographic distance of 2.5 Å, the single van der Waals term adds a sizable energetic penalty of 5 kcal mol^{-1} to the overall potential energy function (N.B.: the hydroxylic hydrogen does not participate in van der Waals interactions in the AMBER or GAFF force fields). Ostensibly, KSI utilizes a delicate network of interactions in order to offset the putative 4.5 kcal mol^{-1} penalty imposed by the close $O_{19\text{-}NT}\bullet\bullet\bullet O_{Tyr16}$ distance, though the AMBER force field apparently does not reproduce this correctly.

On the other hand, MD simulations confirmed the expectation that in frames where 19-nortestosterone *was* in close contact with Tyr16 ($O_{19\text{-}NT}\bullet\bullet\bullet O_{Tyr16}$ distance < 3 Å) such as between 6 and 8 ns (fig. S8C), the electric field experienced by C=O was quite large (between –90 and –120 MV/cm), as can be readily seen by comparing to the same time window in fig. S8A. This observation suggests that fixed charges can approximately reproduce the extreme electric fields given the correct geometry, although it is quite likely *accurate* models of active site electric fields will require a higher-level treatment (e.g., explicit polarization or a QM/MM treatment).

In principle, this difficulty could have been side-stepped by applying a restraint to the O•••O distance – forcing it to remain close to the crystallographic value – or by pre-

selecting a reaction coordinate of interest and freezing the other degrees of freedom. These strategies would invariably lead to larger electric fields at C=O and better agreement between computation and experiment. We emphasize that the infrared experiments on KSI•19-nortestosterone described in this paper were performed in the steady-state, implying that the extreme electric fields detected correspond to a typical KSI•19-nortestosterone configuration in thermal equilibrium, ***not*** *to some rare excursion of the field due to a fluctuation*. In fact, the narrow linewidth of the C=O peak observed in WT KSI (Fig. 3A) suggests *prima facie* that the enzyme makes fluctuations *away* from the extreme electric field very rare. This reveals an important aspect about the nature of KSI's catalysis: rather than transiently sampling the catalytically conducive state (corresponding to extreme electric fields at the C=O bond, and to short $O_{19\text{-}NT}$•••O_{Tyr16} distances of ca. 2.5 Å), KSI maintains it at equilibrium. In other words, the catalytic power of KSI originates in its ability to bias the sampling of configurations to favor those that are catalytically conducive (which may otherwise be only rarely sampled in solution) (*70*).

Supplementary Figures:

A

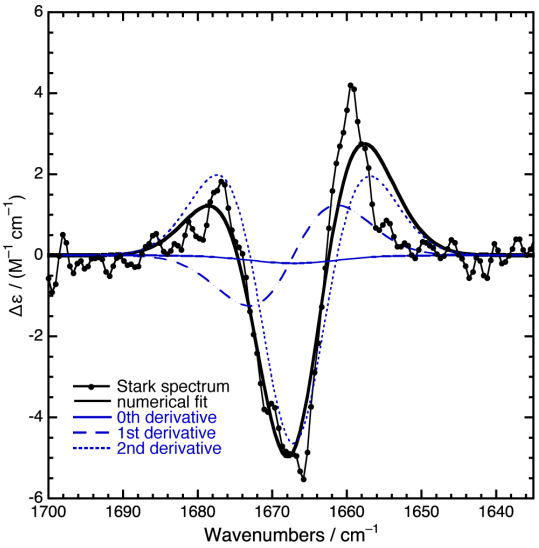

B

	absorption			Stark			
	peak position (cm^{-1})	FWHM (cm^{-1})	peak area ($M^{-1}cm^{-2}$)	*A*	*B* (cm^{-1})	*C* (cm^{-2})	$\|\Delta\mu\|f$ (cm^{-1}/(MV/cm))
raw absorption	1666.3	13.8	13,000	carried out analysis on fit of the raw absorbance			
fit	1667.2	14.0	12,600	$1 \pm 0.3 \times 10^{-4}$	$5.4 \pm 3 \times 10^{-3}$	$1.92 \pm 0.19 \times 10^{-1}$	1.39 ± 0.05

Fig. S1. Analysis of 19-nortestosterone's vibrational Stark effect. (**A**) Stark spectrum (dotted black trace) at a field of 1.0 MV/cm of the C=O vibration of 19-nortestosterone (50 mM) dissolved in 2-methyl tetrahydrofuran at 77 K (reproduced from Fig. 2B). The decomposition of the numerical fit (thick black trace) to the derivative components (blue traces) is shown. The Stark spectrum is dominated by the contribution of the second derivative, which implies that the vibration's sensitivity to electric fields is mostly linear, arising from the difference dipole. (**B**) Fitting parameters for the Stark spectrum, corresponding to the contributions from the 0th (*A*), 1st (*B*), and 2nd (*C*) derivative components respectively. Values and errors are the mean and std. dev. over three repeats. The difference dipole is a derived quantity from the second derivative component, and assumes the angle between the vibration's difference dipole and transition dipole is 0˚. This assumption is expected to hold for localized oscillators with 1-dimensional behavior, and has been shown to be the case previously (*6*).

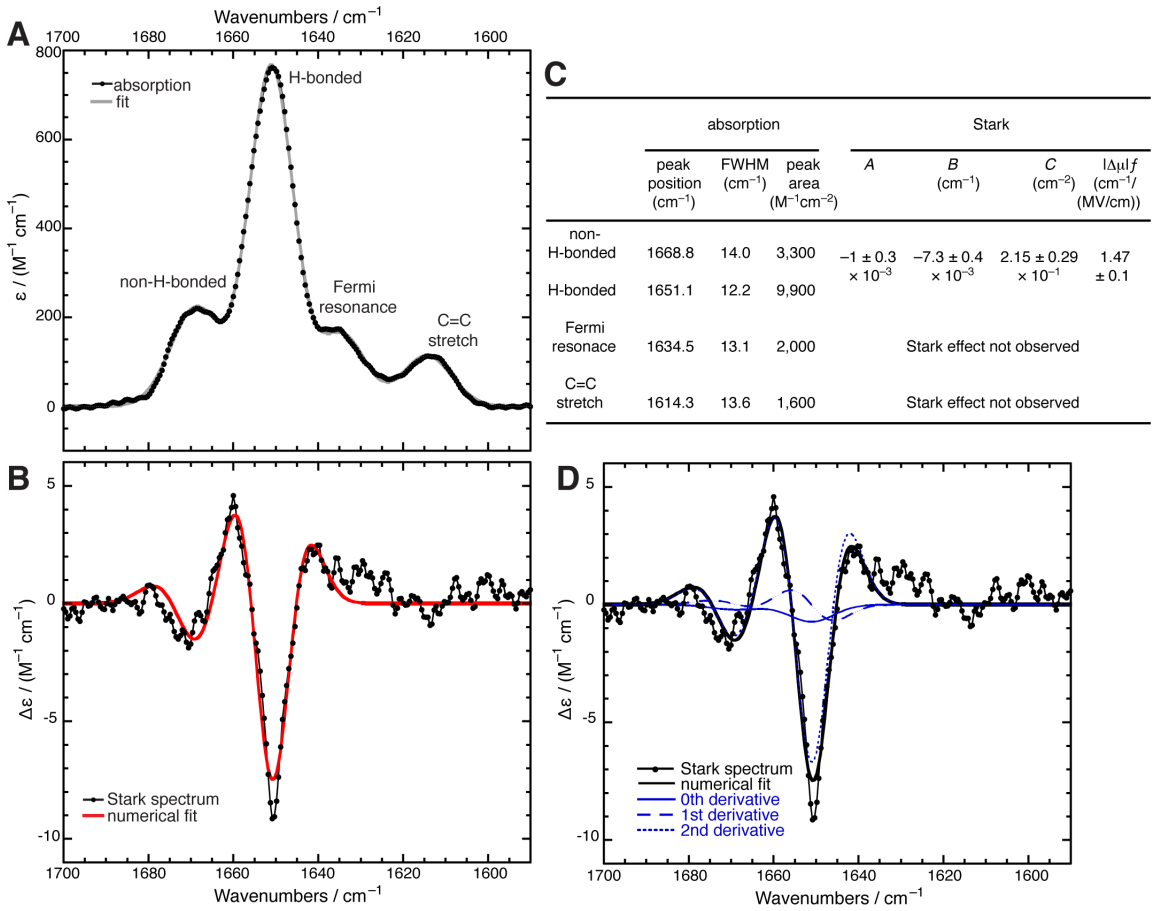

C

	absorption			Stark			
	peak position (cm^{-1})	FWHM (cm^{-1})	peak area ($M^{-1}cm^{-2}$)	*A*	*B* (cm^{-1})	*C* (cm^{-2})	$\|\Delta\mu\|f$ (cm^{-1}/(MV/cm))
non-H-bonded	1668.8	14.0	3,300	$-1 \pm 0.3 \times 10^{-3}$	$-7.3 \pm 0.4 \times 10^{-3}$	$2.15 \pm 0.29 \times 10^{-1}$	1.47 ± 0.1
H-bonded	1651.1	12.2	9,900				
Fermi resonace	1634.5	13.1	2,000	Stark effect not observed			
C=C stretch	1614.3	13.6	1,600	Stark effect not observed			

Fig. S2. Stark spectroscopy of 19-nortestosterone when hydrogen bonded. (**A**) Absorption spectrum of 19-nortestosterone (100 mM) in glassy ethanol at 77 K. The main peak (at 1651 cm^{-1}) is red-shifted about 15 cm^{-1} relative to the C=O band in 2-methyl tetrahydrofuran, consistent with a hydrogen bonding interaction. The smaller band at 1669 cm^{-1} is assigned to a non-hydrogen-bonded population since it possesses a similar wavenumber as the C=O band in 2-methtyl tetrahydrofuran (fig. S1). The two small bands at 1634 cm^{-1} and 1614 cm^{-1} are a Fermi resonance and the C=C stretch respectively. (**B**) Stark spectrum at a field of 0.9 MV/cm (scaled to 1 MV/cm). (**C**) Fitting parameters for the Stark spectrum. Values and errors are the mean and std. dev. over three repeats. (**D**) Decomposition of the numerical fit (thick black trace) to the derivative components (blue traces). In both 2-methyl tetrahydrofuran and ethanol, the C=O vibration's Stark band is strongly second derivative in nature, leading to similar values for the Stark tuning rate (**C**). The two Stark features corresponding to C=O (with and without a hydrogen

bond) are well fit to a common set of fitting parameters, supporting the assignment to C=O and the claim that hydrogen bonding minimally affects the vibration's Stark properties. The Fermi resonance and C=C stretch do not produce observable Stark effects, implying that their frequencies do not respond sensitively to electric fields (consistent with the observation in Fig. 2C that the band's frequency is not strongly affected by solvent variation).

A

Solvent	Color	Dielectric Constant	Calculated Electric Field (MV/cm)	
			mean	std. dev.
n-hexane		1.89	–0.07 ± 0.03	0.9
dibutyl ether		4.34	–8.9 ± 0.5	5.4
tetrahydrofuran		7.43	–18.5 ± 0.3	8.0
valeronitrile		20.04	–22.1 ± 0.3	8.6
acetonitrile		37.5	–31.3 ± 0.2	11.2
dimethyl sulfoxide		46.84	–32.5 ± 0.4	10.8
dichloromethane		8.93	–36.9 ± 0.4	13.4
chloroform		4.71	–37.4 ± 1.2	17.7
water		78.54	–80.4 ± 2.0	35

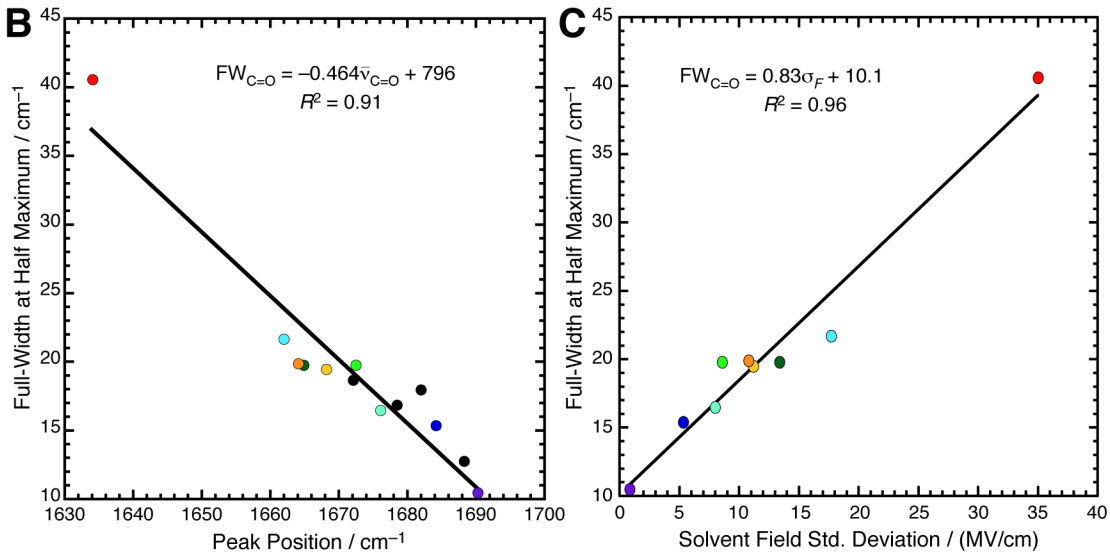

Fig. S3. MD simulations of solvent fields and linewidth analysis. (**A**) The mean and standard deviation of the distribution of electric fields experienced by the carbonyl group of 19-nortestosterone in various organic solvents and water. The electric field is defined as the average between the C- and O-atoms of the projections of the solvent field along the CO bond vector. As shown in Fig. 2D, there is a strong correlation between the peak position and the mean solvent field. (**B**) Plot of full-width at half-maximum of 19-nortestosterone's C=O band against the central frequency of the band across a series of solvents demonstrates a clear correlation (R^2 = 0.91). The trend can be qualitatively explained by noting that a solvent which exerts larger electric fields (resulting in a more red-shifted peak frequency) will also produce a more heterogeneous

distribution of electric fields (resulting in a broader peak). While this qualitative relationship holds across a series of solvents, it very clearly breaks down upon considering the C=O bands of 19-nortestosterone bound to KSI (Fig. 3A, table S2), which were all very narrow though substantially red-shifted. This observation supports the hypothesis that an enzyme active site supplies a relatively rigid environment whose dynamic characteristics qualitatively differ from those of disordered solvation environments. (**C**) C=O linewidth is well explained (R^2 = 0.96) by the standard deviation of the electric field distribution across the solvent series, providing evidence in support of the notion that linewidth encodes information about a given environment's degree of electric field heterogeneity. For reference, the lifetime-limited linewidth of a typical C=O vibration (ca. 1–2 ps) is between 5 and 2.5 cm^{-1}.

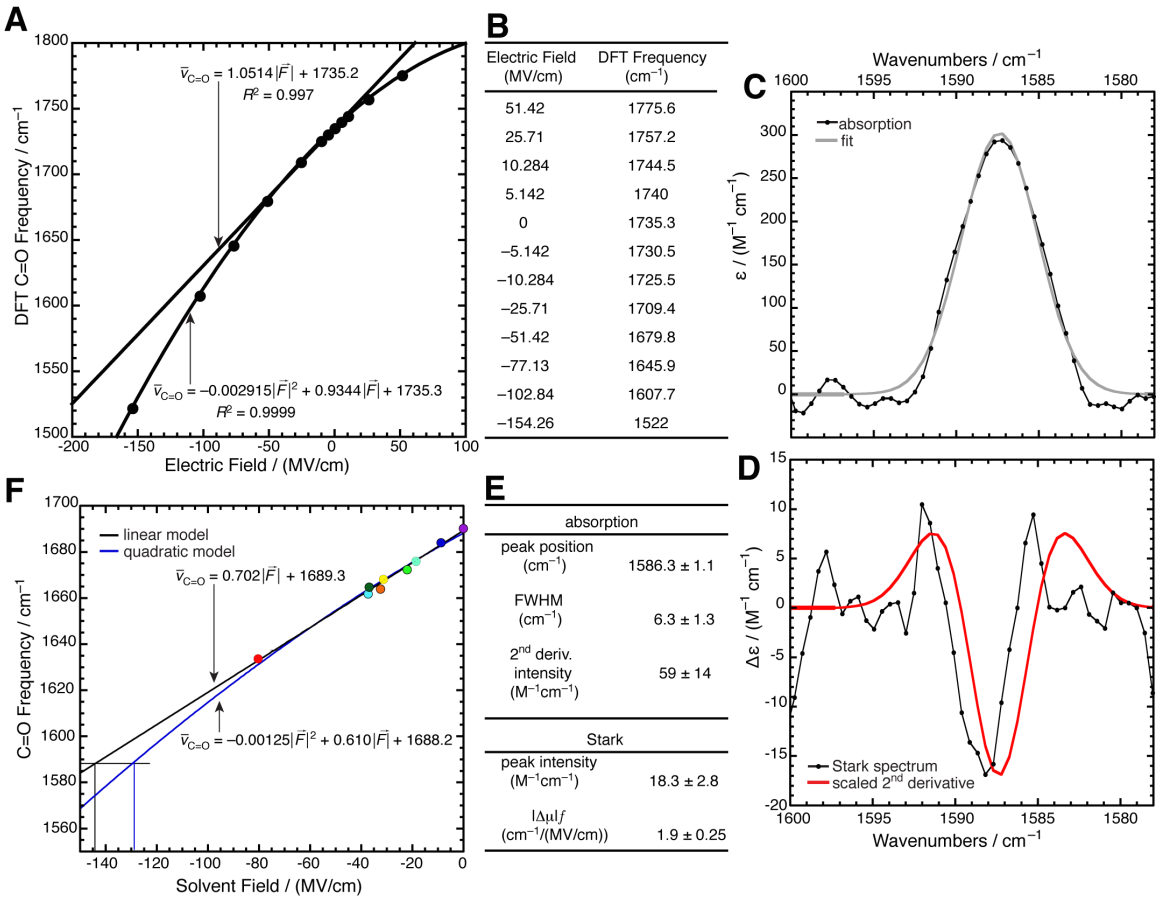

Fig. S4. Quadratic vibrational Stark effects. (**A**) DFT-calculated anharmonic frequency of 19-nortestosterone in the presence of varying electric fields (applied *in silico*) along the C=O axis. Between –50 and +25 MV/cm, frequency varies linearly with field; outside this interval, frequency variation is better described with a quadratic model. (**B**) Frequencies used to construct panel A. (**C**) Absorption spectrum of 19-nortestosterone sulfate bound to WT KSI (4 mM) in a vitrified mixture of 1:1 buffered D_2O:glycerol-d_3 at 77 K. The primary band (at 1586 cm^{-1}) is not shifted with respect to its position at room temperature. (**D**) Stark spectrum at a field of 0.9 MV/cm (scaled to 1 MV/cm). Shown superimposed is the rescaled 2nd derivative of the fit to the low-temperature absorption; the scaling parameter is used to estimate the difference dipole. (**E**) Fitting parameters for the Stark spectrum. Values and errors are the mean and std. dev. over three repeats. (**F**) A quadratic field-frequency model (blue trace) derived from the dependence of 19-nortestosterone's difference dipole on its environment's electric field (see text S2). The

quadratic model is approximately linear between fields of 0–80 MV/cm, and so describes the trends in solvent-induced frequency shifts identically to the linear model (Fig. 2D, black trace). However, at large electric fields, the parabolic character is non-negligible. The lines in the bottom-left corner illustrate that the C=O frequency of 19-nortestosterone in WT KSI (1588 cm^{-1}) corresponds to a field of –144 MV/cm in the original linear model, but to a slightly smaller field of –129 MV/cm in the quadratic model (see fig. S7A).

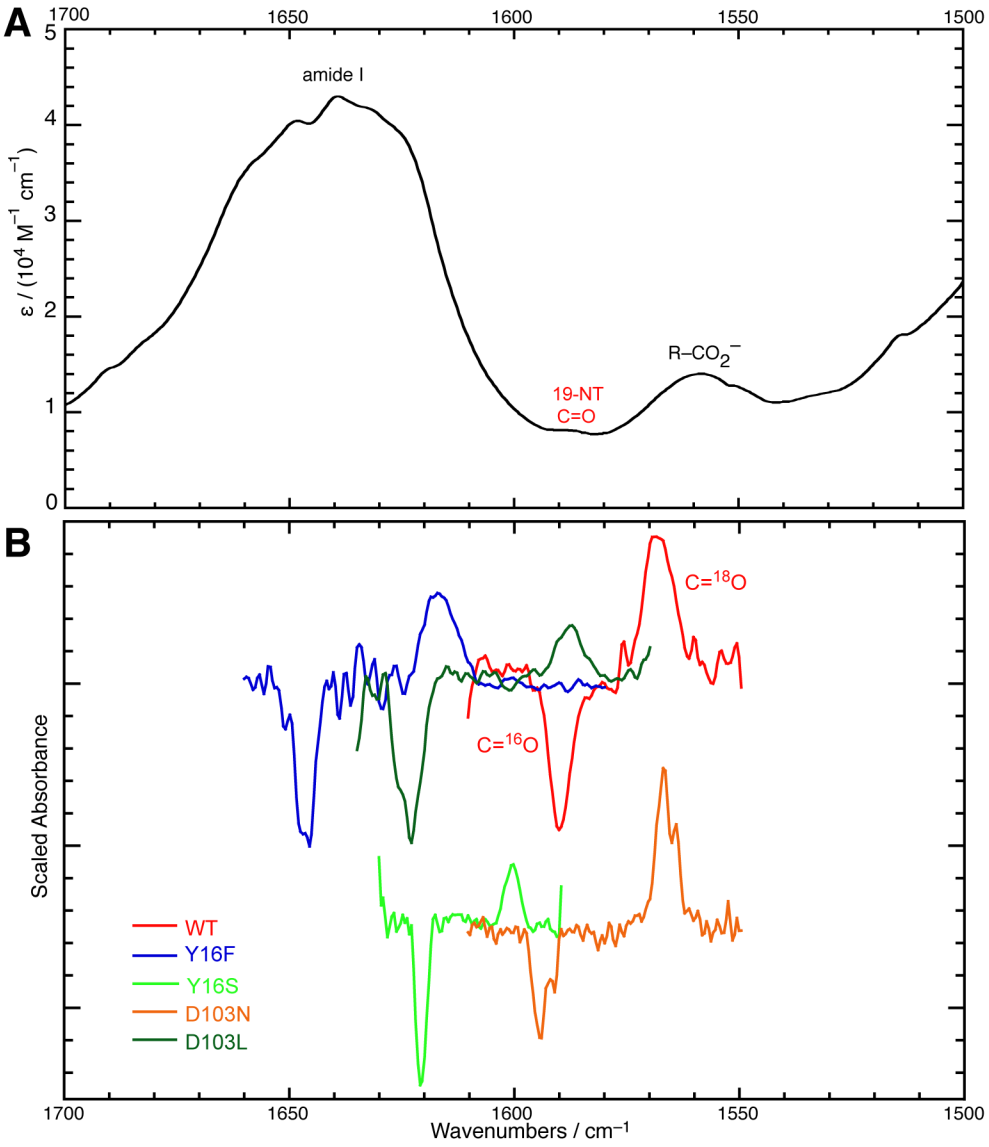

Fig. S5. FT-IR spectra of [^{18}O]19-nortestosterone sulfate bound to KSI and mutants. (**A**) Raw absorption spectrum of WT KSI•19-nortestosterone at 77 K, illustrating the amide background and its absorptivity relative to the C=O vibrational probe. KSI possesses a fairly standard IR absorption spectrum for a protein (top right), with a large amide I band peaked at 1640 cm^{-1}. The band near 1550 cm^{-1} is a superposition of vibrations arising from side-chains, but is likely mostly due to the anti-symmetric carboxylate stretches of Asp's and Glu's. (**B**) Difference IR spectra acquired by subtracting the spectrum of KSI•19-nortestosterone sulfate from the spectrum of KSI•[^{18}O]19-nortestosterone sulfate for WT KSI and the four mutants studied. Positive bands correspond to the C=^{18}O stretch and negative bands correspond to the

C=^{16}O stretch – frequencies, linewidths, and errors are compiled in table S2. Spectra for Y16S and D103N displaced for clarity. The differences in the linewidth and intensity between C=^{16}O and C=^{18}O bands are likely due to baseline error resulting from the fact that the amide background from KSI is higher in different parts of the spectral region. The differences in isotope shifts among mutants are likely due to a Fermi resonance in the region.

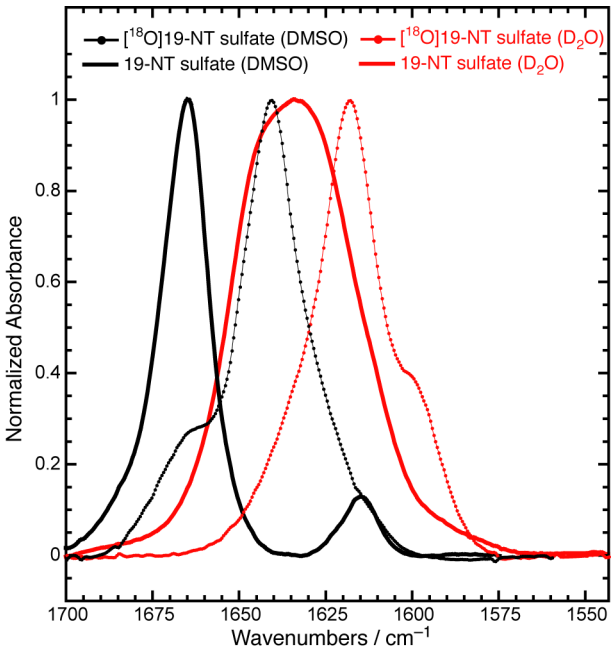

Fig. S6. FT-IR spectra of [^{18}O]19-nortestosterone sulfate. 19-nortestosterone sulfate, dissolved in either dimethyl sulfoxide (DMSO, black) or water (red) in both its natural abundance (solid) and ^{18}O enriched isotopomer (dotted). The isotope shift in DMSO is 24 cm^{-1}, but only 15 cm^{-1} in water. Isotopic substitution causes the C=O band to narrow significantly in water, but broaden slightly in DMSO. These phenomena are possibly due to Fermi resonances (appear in spectra as side bands), which can shift and change the intensity of the C=O band in an isotope-dependent manner. This observation helps explain the isotope studies in KSI (fig. S5) in which isotopic substitution has a non-uniform effect on the C=^{18}O minus C=^{16}O frequency difference in different mutant backgrounds.

A

Mutant	Free Energy Barrier (kcal mol^{-1})	Active Site Electric Field: Linear Model (MV/cm)	Active Site Electric Field: Quadratic Model (MV/cm)
WT	11.5 ± 0.08	−144 ± 6	−129
Y16F	16.0 ± 0.08	−60 ± 3	−59
Y16S	13.6 ± 0.05	−96 ± 4	−92
D103N	12.3 ± 0.03	−134 ± 4	−122
D103L	14.2 ± 0.02	−92 ± 4	−88
D40N	20.0 ± 0.03	−135 ± 4	−123

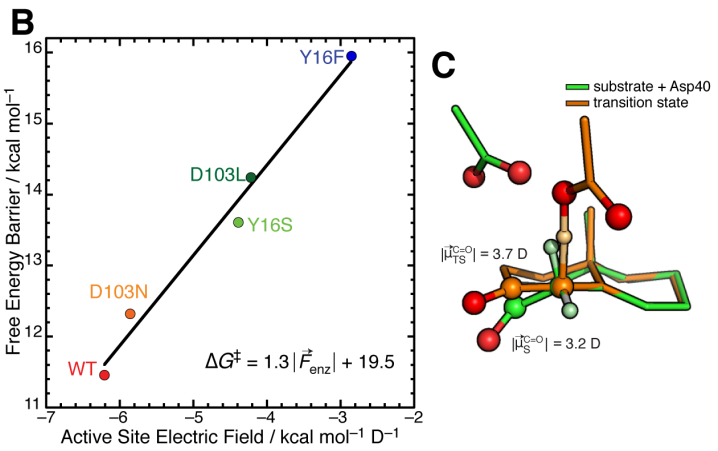

Fig. S7. Effect of quadratic Stark effect on electrostatic catalysis model. (**A**) The free energy barriers for the conversion of 5-androstene to 4-androstene by WT KSI and mutants, and those enzymes' active site electric fields. The active site electric fields are determined from the vibrational frequencies (table S2) using either a linear field-frequency model (Fig. 2D) or a quadratic field-frequency model (fig. S4F). The conversion factor between MV/cm and kcal mol^{-1} D^{-1} is 0.04798. (**B**) The use of a quadratic model to derive active site electric fields does not appreciably alter the catalytic model from Fig. 3, B and C. Replotting the catalytic data with the updated electric field values admits a regression line (in blue) with a slightly larger slope and intercept ($\Delta G^{\ddagger} = 1.27\left|\vec{F}_{\text{enz}}\right| + 19.5$) and an identical correlation coefficient (R^2 = 0.98). The original rate-field trend line is shown in black for comparison. Although the quadratic model assigns WT KSI a lower electric field, it predicts a larger overall electrostatic contribution to catalysis because of the larger value of $\left|\Delta\vec{\mu}_{\text{rxn}}\right|$. (**C**) Structural and electrostatic changes that accompany formation of the transition state (Asp40 is shown *above* the substrate for clarity), based on *ab initio* calculations in the gas phase. The DFT-calculated value for $\left|\Delta\vec{\mu}_{\text{rxn}}\right|$ is 0.5 D (table S3).

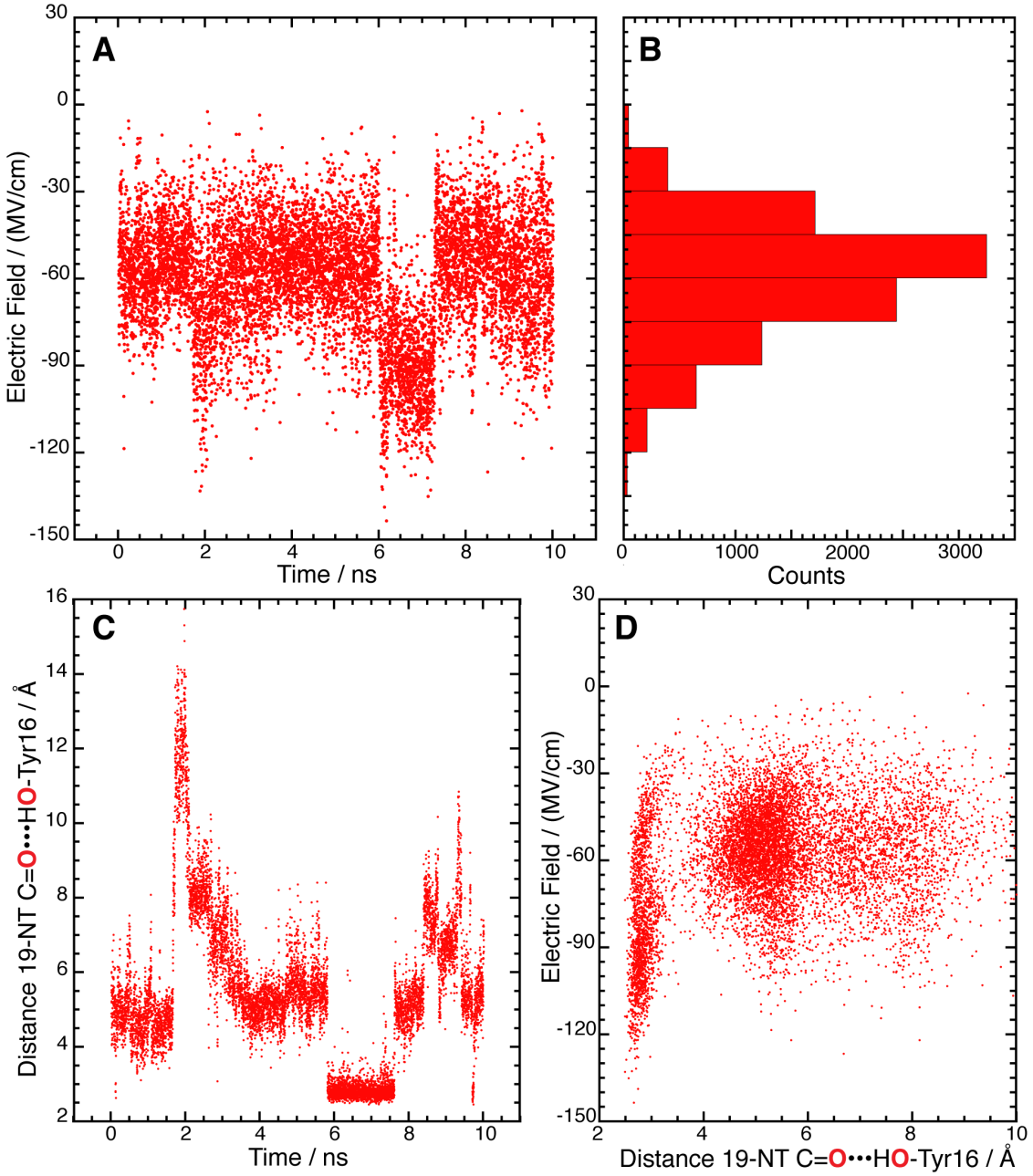

Fig. S8. MD simulations of 19-nortestosterone bound to KSI. (**A**) The electric field experienced by the C=O vibration of 19-NT during a 10-ns trajectory in wild-type KSI. (**B**) The associated electric field histogram has an asymmetric distribution with a noticeable tail at high electric fields. (**C**) Trajectory of the distance between the carbonyl O of 19-NT and the hydroxylic O of Tyr16 (d_{OO}) in WT KSI•19-NT. The simulation samples a

wide distribution of distances with various residency times, but between t = 6 ns and t = 8 ns, the 19-NT molecule returns to a geometry resembling the crystal structure with a short d_{OO}. (**D**) Correlation plot showing the relationship between the electric field experienced by the carbonyl of 19-NT in WT KSI and d_{OO}. The plot shows that snapshots associated with large electric fields (< –90 MV/cm) most frequently occur when d_{OO} < 4 Å.

Supplementary Tables:

Table S1. Spectral data for vibrational solvatochromism of 19-nortestosterone. All samples were at 10 mM concentration, and spectra were obtained at room temperature. Frequencies in this table correspond to the C=O stretching mode, which has some contribution from the conjugated C=C. In most of these solvents, the C=C mode (which has some C=O contribution) is observed between 1615–1620 cm^{-1}. In contrast with the C=O mode, the C=C mode's frequency does not vary strongly or consistently with solvent polarity (Fig. 2C). Center frequencies and full-width at half maxima (FWHM) were determined using two methods. For analysis, the data obtained with peak picking were used; however, their similarity to the values obtained with curve fitting attests to the robustness of the spectral data.

		Peak Picking		Curve Fitting	
Solvent	Dielectric Constant*	Peak Position (cm^{-1})	FWHM (cm^{-1})	Peak Position (cm^{-1})	FWHM (cm^{-1})
hexanes	1.89	1690.2	10.5	1689.7	10.1
cyclohexane	2.02	1688.2	12.8	1686.9	13.2
dibutylether	3.08	1684.1	15.4	1684	15.2
diethylether	4.34	1681.9	18	1680.8	18.3
chloroform	4.71	1661.9	21.7	1663.9	23.8
2-methyl-tetrahydrofuran	6.97	1678.4	16.9	1678.8	17.3
tetrahydrofuran	7.43	1676	16.5	1676.9	17.9
dichloromethane	8.93	1664.8	19.8	1666.5	21
valeronitrile	20.04	1672.4	19.8	1672.1	21.3
butyronitrile	24.83	1672	18.7	1671.9	20
acetonitrile	37.5	1668.1	19.5	1668.2	20.6
dimethylsulfoxide	46.84	1664	19.9	1664.9	22.2
dimethylsulfoxide†	46.84	1664.7	18.1	1665.7	16.7
D_2O†	78.54	1634	40.6	1633.7	39.5

*The static dielectric constant at 25 ˚C. According to continuum dielectric theory, the dielectric constant is related to the solvent's reaction field (i.e., solvent field); concomitantly, a strong correlation between increasing dielectric constant and decreasing frequency is observed. †These two entries correspond to data for 19-nortestosterone sulfate. 19-nortestosterone sulfate is

soluble in water (19-nortestosterone is not), allowing the addition of an important solvent to the study. Dimethylsulfoxide is the only solvent in which both steroids are soluble, permitting one to observe that the two molecules possess similar C=O stretching frequency when in similar environments.

Table S2. Spectral data for 19-nortestosterone sulfate bound to WT KSI and mutants.

Samples were prepared by combining 19-nortestoserone sulfate (or its isotopologue) with KSI (or mutant) to form a complex, with final concentrations around 3 mM and 4 mM, respectively.

	19-nortestosterone sulfate*			[^{18}O]19-nortestosterone sulfate*				
		Curve Fitting			Curve Fitting			
Mutant	n †	Peak Position (cm^{-1})	FWHM (cm^{-1})	n †	Peak Position (cm^{-1})	FWHM (cm^{-1})	Isotope Shift (cm^{-1})	k_{cat} ‡ (s^{-1})
WT	13	1588.3 ± 2.4	6.5 ± 2.6	6	1564.7 ± 3.0	9.5 ± 2.8	23.6	$(2.43 \pm 0.34) \times 10^{4}$
Y16F	7	1647.5 ± 1.3	6.3 ± 3.5	2	1617.2 ± 1.0	8.7 ± 0.6	30.3	$(1.2 \pm 0.2) \times 10^{1}$
Y16S	8	1621.9 ± 1.3	4.3 ± 1.3	3	1600.4 ± 0.1	4.1 ± 0.7	21.5	$(6.4 \pm 0.6) \times 10^{2}$
D103N	5	1595.1 ± 0.6	7.4 ± 2.3	2	1566.2 ± 0.5	3.9 ± 1.8	28.9	$(5.7 \pm 0.3) \times 10^{3}$
D103L	7	1624.9 ± 1.6	5.1 ± 1.0	2	1587.6 ± 0.1	6.2 ± 0.3	37.3 §	$(2.2 \pm 0.1) \times 10^{2}$
D40N	4	1594.4 ± 0.4	2.4 ± 0.5					$(1.8 \pm 0.1) \times 10^{-2}$

*The [^{18}O]19-nortestosterone sulfate band was observed by referencing against an identical sample except replacing [^{18}O]19-nortestosterone sulfate with its natural abundance isotopologue. For natural abundance 19-nortestosterone sulfate, the peak was observed either through ligand editing (using equilenin as the ligand in the reference) or through isotope editing (using the negative band from the experiments with [^{18}O]19-nortestosterone sulfate). †For each mutant and isotopologue, the C=O band was observed and recorded n times. The values and errors given for peak positions and full-widths at half maximum (FWHM) are the means and standard deviations from the distribution of independent measurements. ‡k_{cat} from Michaelis-Menten kinetics of each mutant with the steroid 5-androstene-3,17-dione as substrate. Values taken from literature (*16*, *18*, *19*). § The larger than expected isotope shift may be explained by considering Fermi resonance effects, see fig. S6.

Table S3. *Ab initio* electrostatic properties of reaction states. Charges and bond dipoles of the C=O bond in the substrate (reactant) state and in the transition state corresponding to the first chemical step of KSI's mechanism (Fig. 1B), according to two population analysis methods. All calculations carried out by density functional theory at the B3LYP/6–311++G** level in the gas phase. Illustrations of the optimized structures corresponding to the reaction state and transition state are shown in fig. S7C.

		Reactant state	Transition state	Product state
C=O bond length (Å)		1.219	1.24	1.255
CHelpG	C charge (*e*)	0.5721	0.5879	0.7016
	O charge (*e*)	–0.5381	–0.5669	–0.8154
	CO dipole (D)	3.25	3.44	4.57
Merz-Kollman	C charge (*e*)	0.5035	0.5348	0.5889
	O charge (*e*)	–0.5963	–0.7060	–0.7692
	CO dipole (D)	3.22	3.69	4.09

References

1. R. M. Pollack, Enzymatic mechanisms for catalysis of enolization: Ketosteroid isomerase. *Bioorg. Chem.* **32**, 341–353 (2004). Medline doi:10.1016/j.bioorg.2004.06.005

2. D. C. Hawkinson, T. C. Eames, R. M. Pollack, Energetics of 3-oxo-Δ^5-steroid isomerase: Source of the catalytic power of the enzyme. *Biochemistry* **30**, 10849–10858 (1991). Medline doi:10.1021/bi00109a007

3. D. A. Kraut, P. A. Sigala, B. Pybus, C. W. Liu, D. Ringe, G. A. Petsko, D. Herschlag, Testing electrostatic complementarity in enzyme catalysis: Hydrogen bonding in the ketosteroid isomerase oxyanion hole. *PLOS Biol.* **4**, e99 (2006). Medline doi:10.1371/journal.pbio.0040099

4. S. C. L. Kamerlin, P. K. Sharma, Z. T. Chu, A. Warshel, Ketosteroid isomerase provides further support for the idea that enzymes work by electrostatic preorganization. *Proc. Natl. Acad. Sci. U.S.A.* **107**, 4075–4080 (2010). Medline doi:10.1073/pnas.0914579107

5. D. Herschlag, A. Natarajan, Fundamental challenges in mechanistic enzymology: Progress toward understanding the rate enhancements of enzymes. *Biochemistry* **52**, 2050–2067 (2013). Medline doi:10.1021/bi4000113

6. S. G. Boxer, Stark realities. *J. Phys. Chem. B* **113**, 2972–2983 (2009). Medline doi:10.1021/jp8067393

7. S. S. Andrews, S. G. Boxer, Vibrational Stark effects of nitriles I. Methods and experimental results. *J. Phys. Chem. A* **104**, 11853–11863 (2000). doi:10.1021/jp002242r

8. A. J. Stafford, D. M. Walker, L. J. Webb, Electrostatic effects of mutations of Ras glutamine 61 measured using vibrational spectroscopy of a thiocyanate probe. *Biochemistry* **51**, 2757–2767 (2012). Medline doi:10.1021/bi201225p

9. A. T. Fafarman, P. A. Sigala, D. Herschlag, S. G. Boxer, Decomposition of vibrational shifts of nitriles into electrostatic and hydrogen-bonding effects. *J. Am. Chem. Soc.* **132**, 12811–12813 (2010). Medline doi:10.1021/ja104573b

10. C. T. Liu, J. P. Layfield, R. J. Stewart 3rd, J. B. French, P. Hanoian, J. B. Asbury, S. Hammes-Schiffer, S. J. Benkovic, Probing the electrostatics of active site microenvironments along the catalytic cycle for *Escherichia coli* dihydrofolate reductase. *J. Am. Chem. Soc.* **136**, 10349–10360 (2014). Medline doi:10.1021/ja5038947

11. A. Kuliopulos, A. S. Mildvan, D. Shortle, P. Talalay, Kinetic and ultraviolet spectroscopic studies of active-site mutants of delta 5-3-ketosteroid isomerase. *Biochemistry* **28**, 149–159 (1989). Medline doi:10.1021/bi00427a022

12. M. A. Massiah, C. Abeygunawardana, A. G. Gittis, A. S. Mildvan, Solution structure of Δ^5-3-ketosteroid isomerase complexed with the steroid 19-nortestosterone hemisuccinate. *Biochemistry* **37**, 14701–14712 (1998). Medline doi:10.1021/bi981447b

13. S. D. Fried, L.-P. Wang, S. G. Boxer, P. Ren, V. S. Pande, Calculations of the electric fields in liquid solutions. *J. Phys. Chem. B* **117**, 16236–16248 (2013). Medline doi:10.1021/jp410720y

14. S. D. Fried, S. Bagchi, S. G. Boxer, Measuring electrostatic fields in both hydrogen-bonding and non-hydrogen-bonding environments using carbonyl vibrational probes. *J. Am. Chem. Soc.* **135**, 11181–11192 (2013). Medline doi:10.1021/ja403917z

15. W. Childs, S. G. Boxer, Solvation response along the reaction coordinate in the active site of ketosteroid isomerase. *J. Am. Chem. Soc.* **132**, 6474–6480 (2010). Medline doi:10.1021/ja1007849

16. S. W. Kim, K. Y. Choi, Identification of active site residues by site-directed mutagenesis of Δ^5-3-ketosteroid isomerase from *Pseudomonas putida* biotype B. *J. Bacteriol.* **177**, 2602–2605 (1995). Medline

17. G. H. Nam, D. S. Jang, S. S. Cha, T. H. Lee, D. H. Kim, B. H. Hong, Y. S. Yun, B. H. Oh, K. Y. Choi, Maintenance of α-helical structures by phenyl rings in the active-site tyrosine triad contributes to catalysis and stability of ketosteroid isomerase from *Pseudomonas putida* biotype B. *Biochemistry* **40**, 13529–13537 (2001). Medline doi:10.1021/bi015547k

18. D. A. Kraut, P. A. Sigala, T. D. Fenn, D. Herschlag, Dissecting the paradoxical effects of hydrogen bond mutations in the ketosteroid isomerase oxyanion hole. *Proc. Natl. Acad. Sci. U.S.A.* **107**, 1960–1965 (2010). Medline doi:10.1073/pnas.0911168107

19. G. Choi, N. C. Ha, M. S. Kim, B. H. Hong, B. H. Oh, K. Y. Choi, Pseudoreversion of the catalytic activity of Y14F by the additional substitution(s) of tyrosine with phenylalanine in the hydrogen bond network of Δ^5-3-ketosteroid isomerase from *Pseudomonas putida* biotype B. *Biochemistry* **40**, 6828–6835 (2001). Medline doi:10.1021/bi002767+

20. A. Warshel, Energetics of enzyme catalysis. *Proc. Natl. Acad. Sci. U.S.A.* **75**, 5250–5254 (1978). Medline doi:10.1073/pnas.75.11.5250

21. A. Warshel, P. K. Sharma, M. Kato, Y. Xiang, H. Liu, M. H. Olsson, Electrostatic basis for enzyme catalysis. *Chem. Rev.* **106**, 3210–3235 (2006). Medline doi:10.1021/cr0503106

22. A. Radzicka, R. Wolfenden, A proficient enzyme. *Science* **267**, 90–93 (1995). Medline doi:10.1126/science.7809611

23. W. J. Houck, R. M. Pollack, Temperature effects on the catalytic activity of the D38E mutant of 3-oxo-Δ^5-steroid isomerase: Favorable enthalpies and entropies of activation relative to the nonenzymatic reaction catalyzed by acetate ion. *J. Am. Chem. Soc.* **126**, 16416–16425 (2004). Medline doi:10.1021/ja046819k

24. M. I. Page, W. P. Jencks, Entropic contributions to rate accelerations in enzymic and intramolecular reactions and the chelate effect. *Proc. Natl. Acad. Sci. U.S.A.* **68**, 1678–1683 (1971). Medline doi:10.1073/pnas.68.8.1678

25. J. R. Knowles, Enzyme catalysis: Not different, just better. *Nature* **350**, 121–124 (1991). Medline doi:10.1038/350121a0

26. J. C. Austin, T. G. Spiro, A. Kuliopulos, A. S. Mildvan, Substrate polarization by residues in Δ^5-3-ketosteroid isomerase probed by site-directed mutagenesis and UV resonance Raman spectroscopy. *Protein Sci.* **1**, 259–270 (1992). Medline doi:10.1002/pro.5560010208

27. P. R. Carey, P. J. Tonge, Unlocking the secrets of enzyme power using Raman spectroscopy. *Acc. Chem. Res.* **28**, 8–13 (1995). doi:10.1021/ar00049a002

28. J. G. Belasco, J. R. Knowles, Direct observation of substrate distortion by triosephosphate isomerase using Fourier transform infrared spectroscopy. *Biochemistry* **19**, 472–477 (1980). Medline doi:10.1021/bi00544a012

29. G. Choi, N. C. Ha, S. W. Kim, D. H. Kim, S. Park, B. H. Oh, K. Y. Choi, Asp-99 donates a hydrogen bond not to Tyr-14 but to the steroid directly in the catalytic mechanism of Δ 5-3-ketosteroid isomerase from *Pseudomonas putida* biotype B. *Biochemistry* **39**, 903–909 (2000). Medline doi:10.1021/bi991579k

30. J. Wang, R. M. Wolf, J. W. Caldwell, P. A. Kollman, D. A. Case, Development and testing of a general amber force field. *J. Comput. Chem.* **25**, 1157–1174 (2004). Medline doi:10.1002/jcc.20035

31. A. Jakalian, D. B. Jack, C. I. Bayly, Fast, efficient generation of high-quality atomic charges. AM1-BCC model: II. Parameterization and validation. *J. Comput. Chem.* **23**, 1623–1641 (2002). Medline doi:10.1002/jcc.10128

32. B. Hess, C. Kutzner, D. van der Spoel, E. Lindahl, GROMACS 4: Algorithms for highly efficient, load-balanced, and scalable molecular simulation. *J. Chem. Theory Comput.* **4**, 435–447 (2008). doi:10.1021/ct700301q

33. C. Caleman, P. J. van Maaren, M. Hong, J. S. Hub, L. T. Costa, D. van der Spoel, Force field benchmark of organic liquids: Density, enthalpy of vaporization, heat capacities, surface tension, isothermal compressibility, volumetric expansion coefficient, and dielectric constant. *J. Chem. Theory Comput.* **8**, 61–74 (2012). Medline doi:10.1021/ct200731v

34. W. L. Jorgensen, J. Chandrasekhar, J. D. Madura, R. W. Impey, M. L. Klein, Comparison of simple potential functions for simulating liquid water. *J. Chem. Phys.* **79**, 926 (1983). doi:10.1063/1.445869

35. T. Darden, D. York, L. Pedersen, Particle mesh Ewald: An N·log(N) method for Ewald sums in large systems. *J. Chem. Phys.* **98**, 10089 (1993). doi:10.1063/1.464397

36. B. Hess, P-LINCS: A parallel linear constraint solver for molecular simulation. *J. Chem. Theory Comput.* **4**, 116–122 (2008). doi:10.1021/ct700200b

37. G. Bussi, D. Donadio, M. Parrinello, Canonical sampling through velocity rescaling. *J. Chem. Phys.* **126**, 014101 (2007). Medline doi:10.1063/1.2408420

38. H. J. C. Berendsen, J. P. M. Postma, W. F. Van Gunsteren, A. DiNola, J. R. Haak, Molecular dynamics with coupling to an external bath. *J. Chem. Phys.* **81**, 3684 (1984). doi:10.1063/1.448118

39. W. F. Van Gunsteren, H. J. C. Berendsen, A leap-frog algorithm for stochastic dynamics. *Mol. Simul.* **1**, 173–185 (1988). doi:10.1080/08927028808080941

40. M. Parrinello, A. Rahman, Crystal structure and pair potentials: A molecular-dynamics study. *Phys. Rev. Lett.* **45**, 1196–1199 (1980). doi:10.1103/PhysRevLett.45.1196

41. Gaussian 09, Revision D.01, M. J. Frisch, G. W. Trucks, H. B. Schlegel, G. E. Scuseria, M. A. Robb, J. R. Cheeseman, G. Scalmani, V. Barone, B. Mennucci, G. A. Petersson, H.

Nakatsuji, M. Caricato, X. Li, H. P. Hratchian, A. F. Izmaylov, J. Bloino, G. Zheng, J. L. Sonnenberg, M. Hada, M. Ehara, K. Toyota, R. Fukuda, J. Hasegawa, M. Ishida, T. Nakajima, Y. Honda, O. Kitao, H. Nakai, T. Vreven, J. A. Montgomery, Jr., J. E. Peralta, F. Ogliaro, M. Bearpark, J. J. Heyd, E. Brothers, K. N. Kudin, V. N. Staroverov, R. Kobayashi, J. Normand, K. Raghavachari, A. Rendell, J. C. Burant, S. S. Iyengar, J. Tomasi, M. Cossi, N. Rega, J. M. Millam, M. Klene, J. E. Knox, J. B. Cross, V. Bakken, C. Adamo, J. Jaramillo, R. Gomperts, R. E. Stratmann, O. Yazyev, A. J. Austin, R. Cammi, C. Pomelli, J. W. Ochterski, R. L. Martin, K. Morokuma, V. G. Zakrzewski, G. A. Voth, P. Salvador, J. J. Dannenberg, S. Dapprich, A. D. Daniels, Ö. Farkas, J. B. Foresman, J. V. Ortiz, J. Cioslowski, D. J. Fox (Gaussian, Inc., Wallingford CT, 2009).

42. P. J. Stephens, F. J. Devlin, C. F. Chabalowski, M. J. Frisch, Ab initio calculation of vibrational absorption and circular dichroism spectra using density functional force fields. *J. Phys. Chem.* **98**, 11623–11627 (1994). doi:10.1021/j100096a001

43. C. M. Breneman, K. B. Wiberg, Determining atom-centered monopoles from molecular electrostatic potentials. The need for high sampling density in formamide conformational analysis. *J. Comput. Chem.* **11**, 361–373 (1990). doi:10.1002/jcc.540110311

44. B. H. Besler, K. M. Merz Jr., P. A. Kollman, Atomic charges derived from semiempirical methods. *J. Comput. Chem.* **11**, 431–439 (1990). doi:10.1002/jcc.540110404

45. C. Adamo, M. Cossi, N. Rega, V. Barone, in *Theoretical Biochemistry: Processes and Properties of Biological Systems, Theoretical and Computational Chemistry*, Vol. 9 (Elsevier, New York, 1990).

46. S. H. Brewer, S. Franzen, A quantitative theory and computational approach for the vibrational Stark effect. *J. Chem. Phys.* **119**, 851 (2003). doi:10.1063/1.1578471

47. G. U. Bublitz, S. G. Boxer, Stark spectroscopy: Applications in chemistry, biology, and materials science. *Annu. Rev. Phys. Chem.* **48**, 213–242 (1997). Medline doi:10.1146/annurev.physchem.48.1.213

48. B. E. Kohler, J. C. Woehl, Measuring internal electric fields with atomic resolution. *J. Chem. Phys.* **102**, 7773 (1995). doi:10.1063/1.469030

49. E. Vauthey, J. Voss, C. De Caro, A. Renn, U. P. Wild, Spectral hole-burning and stark effect: Frequency dependence of the induced dipole moment of a squaraine dye in polymers. *Chem. Phys.* **184**, 347–356 (1994). doi:10.1016/0301-0104(94)00078-6

50. C. J. F. Böttcher, *Theory of Electric Polarization*, 2nd ed. (Elsevier, Amsterdam, 1973).

51. S. Bagchi, S. D. Fried, S. G. Boxer, A solvatochromic model calibrates nitriles' vibrational frequencies to electrostatic fields. *J. Am. Chem. Soc.* **134**, 10373–10376 (2012). Medline doi:10.1021/ja303895k

52. M. Saggu, N. M. Levinson, S. G. Boxer, Direct measurements of electric fields in weak OH···π hydrogen bonds. *J. Am. Chem. Soc.* **133**, 17414–17419 (2011). Medline doi:10.1021/ja2069592

53. I. T. Suydam, C. D. Snow, V. S. Pande, S. G. Boxer, Electric fields at the active site of an enzyme: Direct comparison of experiment with theory. *Science* **313**, 200–204 (2006). Medline doi:10.1126/science.1127159

54. N. M. Levinson, S. D. Fried, S. G. Boxer, Solvent-induced infrared frequency shifts in aromatic nitriles are quantitatively described by the vibrational Stark effect. *J. Phys. Chem. B* **116**, 10470–10476 (2012). Medline doi:10.1021/jp301054e

55. J. E. Gready, G. B. Backsay, N. S. Hush, Finite-field method calculations. IV. Higher-order moments, dipole moment gradients, polarisability gradients and field-induced shifts in molecular properties: Application to N2, CO, CN^-, HCN and HNC. *Chem. Phys.* **31**, 467–483 (1978). doi:10.1016/0301-0104(78)85136-2

56. C. W. Bauschlicher Jr., The effect of an external electric field on the vibrational frequency of CO. *Chem. Phys. Lett.* **118**, 307–310 (1985). doi:10.1016/0009-2614(85)85321-5

57. G. U. Bublitz, S. G. Boxer, Effective polarity of frozen solvent glasses in the vicinity of dipolar solutes. *J. Am. Chem. Soc.* **120**, 3988–3992 (1998). doi:10.1021/ja971665c

58. S. D. Fried, S. G. Boxer, Thermodynamic framework for identifying free energy inventories of enzyme catalytic cycles. *Proc. Natl. Acad. Sci. U.S.A.* **110**, 12271–12276 (2013). Medline doi:10.1073/pnas.1310964110

59. B. Zeng, R. M. Pollack, Microscopic rate constants for the acetate ion catalyzed isomerization of 5-androstene-3,17-dione to 4-androstene-3,17-dione: A model for steroid isomerase. *J. Am. Chem. Soc.* **113**, 3838–3842 (1991). doi:10.1021/ja00010a028

60. W. P. Jencks, *Catalysis in Chemistry and Enzymology* (Dover, New York, 1987).

61. D.-H. Kim, G. H. Nam, D. S. Jang, G. Choi, S. Joo, J. S. Kim, B. H. Oh, K. Y. Choi, Roles of active site aromatic residues in catalysis by ketosteroid isomerase from *Pseudomonas putida* biotype B. *Biochemistry* **38**, 13810–13819 (1999). Medline doi:10.1021/bi991040m

62. A. Warshel, P. K. Sharma, Z. T. Chu, J. Åqvist, Electrostatic contributions to binding of transition state analogues can be very different from the corresponding contributions to catalysis: Phenolates binding to the oxyanion hole of ketosteroid isomerase. *Biochemistry* **46**, 1466–1476 (2007). Medline doi:10.1021/bi061752u

63. L. A. Xue, P. Talalay, A. S. Mildvan, Studies of the mechanism of the Δ^5-3-ketosteroid isomerase reaction by substrate, solvent, and combined kinetic deuterium isotope effects on wild-type and mutant enzymes. *Biochemistry* **29**, 7491–7500 (1990). Medline doi:10.1021/bi00484a019

64. A. Kuliopulos, P. Talalay, A. S. Mildvan, Combined effects of two mutations of catalytic residues on the ketosteroid isomerase reaction. *Biochemistry* **29**, 10271–10280 (1990). Medline doi:10.1021/bi00496a017

65. P. A. Sigala, J. M. M. Caaveiro, D. Ringe, G. A. Petsko, D. Herschlag, Hydrogen bond coupling in the ketosteroid isomerase active site. *Biochemistry* **48**, 6932–6939 (2009). Medline doi:10.1021/bi900713j

66. D. S. Jang, H. J. Cha, S. S. Cha, B. H. Hong, N. C. Ha, J. Y. Lee, B. H. Oh, H. S. Lee, K. Y. Choi, Structural double-mutant cycle analysis of a hydrogen bond network in ketosteroid isomerase from *Pseudomonas putida* biotype B. *Biochem. J.* **382**, 967–973 (2004). Medline doi:10.1042/BJ20031871

67. L. A. Xue, A. Kuliopulos, A. S. Mildvan, P. Talalay, Catalytic mechanism of an active-site mutant (D38N) of Δ^5-3-ketosteroid isomerase. Direct spectroscopic evidence for dienol intermediates. *Biochemistry* **30**, 4991–4997 (1991). Medline doi:10.1021/bi00234a022

68. S. W. Kim, S. S. Cha, H. S. Cho, J. S. Kim, N. C. Ha, M. J. Cho, S. Joo, K. K. Kim, K. Y. Choi, B. H. Oh, High-resolution crystal structures of Δ^5-3-ketosteroid isomerase with and without a reaction intermediate analogue. *Biochemistry* **36**, 14030–14036 (1997). Medline doi:10.1021/bi971546+

69. K. Lindorff-Larsen, S. Piana, K. Palmo, P. Maragakis, J. L. Klepeis, R. O. Dror, D. E. Shaw, Improved side-chain torsion potentials for the Amber ff99SB protein force field. *Proteins* **78**, 1950–1958 (2010). Medline

70. T. C. Bruice, S. J. Benkovic, Chemical basis for enzyme catalysis. *Biochemistry* **39**, 6267–6274 (2000). Medline doi:10.1021/bi0003689